

Comparing High-Resolution Snow Mapping Approaches in Palsa Mires: UAS LiDAR vs. Modeling

Alexander Störmer^{1,3}, Timo Kumpula^{2,3}, Miguel Villoslada^{2,3,4}, Pasi Korpelainen^{2,3},
Henning Schumacher^{1,3}, and Benjamin Burkhard^{1,3}

¹Institute of Earth System Sciences, Physical Geography and Landscape Ecology, Leibniz University Hannover, Hannover, 30167, Germany

²Department of Geographical and Historical Studies, University of Eastern Finland, Joensuu, 80101, Finland

³Kilpisjärvi Biological Station, University of Helsinki, Kilpisjärvi, 99490, Finland

⁴Institute of Agriculture and Environmental Sciences, Estonian University of Life Sciences, Tartu, Estonia

Correspondence to: Alexander Störmer (stoermer@phygeo.uni-hannover.de)

Abstract. Snow cover has an important role in permafrost processes and dynamics, creating cooling and warming systems, impacting the aggradation and degradation of frozen soil. Despite theoretical, experimental, and remote sensing-based research, comprehensive understanding of small-scaled snow distribution at palsas remains limited. This study compares two approaches to generate spatially continuous, small-scale snow distribution models in palsa mires in northwestern Finland based on Digital Surface Models: a machine learning approach using the Random Forest (RF) algorithm with *in-situ* measured snow depth data and an Unmanned Aerial System (UAS) equipped with a Light Detection and Ranging (LiDAR) sensor. For the first time, snow distribution was recorded over a palsa using a UAS LiDAR data. The aim is to review which approach is more precise-accurate overall and which areas are not represented sufficiently-accurate snow distribution patterns can be identified. In comparison to *in-situ* collected validation data, the machine learning results showed high both the RF results and UAS LiDAR data show sufficient accuracy, with a RMSE of 6.16 cm-18.33 cm (RF) and 23.49 cm (LiDAR) and an R^2 of 0.98, outperforming the LiDAR-based approach, which had an RMSE of 26.73 cm and an R^2 of 0.59. Random Forest models snow distribution significantly better at steep slopes and in vegetated areas. This considerable difference highlights the ability 0.77 respectively 0.691. RF performs particularly well in modeling snow distribution over open water and vegetated areas, demonstrating the potential of machine learning to capture fine-scale snow distribution patterns in detail. However, our results indicate that UAS data enables the study of small-scale patterns based on field observations. The UAS LiDAR also enables a very detailed analysis of the interactions between snow and permafrost interaction at a highly detailed level as well.

Generally, Both approaches reveal snow accumulation zones, especially at steep edges of the palsas and inside cracks are recognizable, while thin snow cover occurs at exposed areas on top of the palsas. Correspondingly, areas with thicker snow cover at the edges and inside cracks act as potential warming spots, possibly leading to heavy degradation including palsa margins and within cracks, where insulation limits frost penetration and contributes to degradation processes such as block erosion. In contrast, areas with thinner snow cover on the exposed crown parts can act as cooling spots. They initially stabilize the frozen core under the crown parts, but then form a thinner snow depth on exposed palsa surfaces allows deeper frost

25 penetration, which initially stabilizes the ice core but leads to the formation of steep edges and ~~expose the frozen core, leading~~
~~finally to even more block erosion and further~~ degradation.

1 Introduction

Snow cover plays an important role in permafrost processes and dynamics. Its physical characteristics impact the aggradation and degradation of frozen soil (Barry, 2002). In March 2023, around 39.26 million km² of the northern hemisphere were
30 permanently or partly covered by snow (NOAA, 2023), affecting around 14.77 million km² permafrost area (Ran et al., 2022). This includes the discontinuous permafrost areas in northern parts of Sweden, Norway and Finland, known as Fennoscandia. Due to changes in climate, a reduction in snow cover duration ~~and an increase in snow depth have been monitored in these~~
~~regions (IPCC, 2023)~~is expected (Quante et al., 2021), leading to changes of air and soil temperature interactions and resulting in negative impacts for permafrost soils (Chen et al., 2021). This has a direct impact on ecological processes, such as a reduced
35 albedo in winter that leads to a higher energy uptake by soils (Thackeray and Fletcher, 2016) and longer growing seasons (Madani et al., 2023). In addition, Wang et al. (2024) showed that snow cover – in combination with landscape heterogeneity - plays an important role in controlling soil temperatures throughout the year. The Intergovernmental Panel on Climate Change (IPCC) already highlighted in their latest report that a loss of permafrost within this century is expected in these regions (IPCC, 2023). ~~Especially in northern Fennoscandia with a main focus on~~In northern Fennoscandia, particularly in northern Finnish
40 Lapland ~~in the main focus of~~ this study - specific periglacial permafrost ~~landform types called palsas are in danger~~landforms known as palsas are at risk of disappearing within this century (Leppiniemi et al., 2023).

The occurrence of palsas, small mounds up to 4 - 7 m height with a frozen core, is bound mainly to the presence of peat-lands and driven by climatic parameters (Meier, 2015; Seppälä, 2011). Palsas serve as indicators of climate warming, as
their degradation and disappearance reflect rising temperatures (Leppiniemi et al., 2023). Additionally, they provide important
45 habitats for various animal species (Luoto et al., 2004) and hold significant cultural and societal value for indigenous and
local communities, particularly in the context of traditional reindeer herding (Markkula et al., 2019). Given their ecological and cultural importance, monitoring their changes is essential. Palsas are highly sensitive to ~~shifts in temperature insulation~~
temperature insulation shifts induced by snow during winter. Their development is directly influenced by ~~the variety of snow~~
~~depth through thermal isolation dynamics~~variations in snow depth, which regulate thermal insulation in winter and ~~protection~~
50 protect against warm air and sunlight in ~~summer, leading to the growth of the~~spring, ultimately affecting Active Layer Thickness (ALT) and ~~warming of the soils~~soil warming (Park et al., 2015; Verdonen et al., 2023, 2024). In ~~detail~~winter, deep snow
~~depth in winter leads to a lower impact on the underlying frozen soil due to a decreased penetration of low temperatures~~
~~, while in summer this would protect the permafrost from thawing~~cover insulates the ground, reducing the penetration of
cold temperatures and keeping the underlying soil comparatively warmer. In summer, this accumulated snow delays ground
55 warming and slows permafrost thawing, resulting in a shallower ALT. These areas are defined as warming areas throughout
this article. They are typically found in depressions, concave terrain, or wind-sheltered locations where snowdrifts accumulate.
Conversely, thin snow cover allows for more intensive winter cooling due to reduced insulation, leading to greater heat loss

from the ground. In summer, these areas warm up earlier, causing a deeper ALT. Such locations are defined as cooling areas. They are commonly found in elevated or wind-exposed areas of the palsa, where snow accumulation is naturally limited (Seppälä, 1982; Olvmo et al., 2020). ~~Lower snow depth would have the exact opposite impact throughout the seasons.~~ This influence on palsas has been empirically demonstrated by Seppälä (2011), who described the impact of variable snow cover on palsa ~~development~~ thermal dynamics during subsequent thawing periods. Moreover, experiments show that mainly the depth of snow cover influences the development of palsas (Seppälä, 1982). Deviations from the usual thickness of snow cover, whether thinner or thicker, induce varying conditions for palsa dynamics. For example, at the steep edges of palsas, the accumulation of snow can pose a risk by destabilizing the frozen core due to increased thermal insulation at these specific areas leading to a higher risk of block erosion (Olvmo et al., 2020; Seppälä, 1994). Despite theoretical, experimental, and remote sensing-based research, comprehensive understanding of actual snow distribution conditions within and around palsas remains limited (Seppälä, 2011; Verdonen et al., 2023). Although they have high potential for accurate mapping, Unmanned Aerial ~~Vehiele~~ Systems (UAS) have not yet been used to measure snow depth in palsa mires.

Consequently, detailed data on snow distribution in palsa mires is not available. Even if sufficient climate data is made available through official weather stations, it is the microclimate inside these mires that impacts the snow distribution in various ways, especially by snow drifts due to strong winds, as monitored ~~exemplarily~~ by Zuidhoff (2002). Since palsa mires occur mostly in remote areas, simple interpolation of climatic observations from weather stations within the same region does not provide data on the actual state within these mire complexes, which does not allow to monitor the exact snow distribution (Verdonen et al., 2023). ~~Microtopography affects snow depth and creates an environment, in which the palsas usually receive enough penetrating cold air to remain stable and to last year after year due to a thin snow cover. However, warming is predicted to increase precipitation in Fennoscandia (IPCC, 2023), leading to higher snow layers in winter, which is detrimental to the palsas and contributes to their thawing. Based on snow depth mapping, identifying cold or warm spots inside palsa mires is possible and can help to improve our understanding of further palsa dynamics.~~ Only *in-situ* measured snow depth data can provide clear insights into these conditions. However, to date and to our knowledge, no small-scale mapping of snow depth in palsa mires has yet been carried out.

Measuring snow depth manually demands a relatively high workload in time and effort under mostly harsh climatic conditions. Thus, measurements of snow depth over a long time span without technical help have been undertaken in Finnish Lapland by only a few researchers, e.g. by Leppänen et al. (2016), who describe the snow survey program by the Finnish Meteorological Institute (FMI) that was established in 1909 in Sodankylä. Statistical evaluations of collected data at weather stations were published for whole Finnish Lapland (Merkouriadi et al., 2017).

The use of remote sensing data and methods to monitor snow depth has become increasingly important in snow research. ~~Satellite data has been widely used for many years to monitor and estimate snow properties such as snow density or snow water equivalent (Holmberg et al., 2024), but only in coarse resolution due to the properties of satellites. Numerous studies have been published recently on methods to determine snow depth with Unmanned Aerial Systems (UAS) in high resolution (cell size of~~ Optical and radar satellite data have been widely utilized to map snow distribution (Marti et al., 2016; Hu et al., 2023), but their coarse resolution limits their effectiveness, particularly in capturing small-scale variations in ground surface conditions.

Small-scale structures, such as palsas, exhibit substantial snow depth heterogeneity, making satellite-derived datasets unsuitable for analyzing these localized processes. To improve spatial resolution, UAS RGB-derived photogrammetry has been increasingly used for high-resolution snow depth mapping. With small grid sizes (10 cm \times 10 cm, respectively or 5 cm \times 5 cm), e.g. by Bühler et al. (2016) and Michele et al. (2016), who directly mapped these methods provide detailed snow depth estimates. Bühler et al. (2016) and Michele et al. (2016) successfully applied this approach to directly map snow depth in alpine terrain using UAS RGB, while Rauhala et al. (2023) and Meriö et al. (2023) compared different UAS in terms of snow depth mapping precision for a test site in Finnish Lapland. They concluded that spatially representative estimates of snow depth can be obtained with UAS. Furthermore, several studies utilizing satellite images to map snow distribution were conducted (Marti et al., 2016; Hu et al., 2023). However, coarse satellite datasets significantly limit the resolution of the results evaluated the accuracy of UAS RGB surveys in Finnish Lapland, showing that they can produce spatially representative snow depth estimates. However, especially to capture the ground surface precisely without vegetation. Small-scale structures such as palsas have very strong changes in snow depth at a fine spatial scale, which limits the information value RGB-derived approaches face challenges in capturing the ground surface, particularly in environments with dense vegetation as suggested by Walker et al. (2021), who explored the accuracy of UAS RGB-derived snow depth mapping and suggested that an approach that better filters out vegetation could improve the mapping results. Recently, UAS equipped with Light Detection and Ranging (LiDAR) sensors have been introduced as an alternative for snow depth monitoring. Unlike RGB sensors, which passively capture optical images, LiDAR actively emits laser pulses and measures their return time to generate high-resolution, three-dimensional surface models. Harder et al. (2020) demonstrated that LiDAR can accurately capture vegetation, allowing for its removal from ground surface data, which significantly improves snow depth estimation. Similarly, Jacobs et al. (2021) showed that LiDAR-based vegetation filtering enhances snow cover mapping in forestry and open areas. Given the limitations of satellite data on resolving small-scale processes in these structures, UAS-based data can provide data to close this gap, but these techniques also have difficulties in mapping the ground surface without vegetation, particularly in subarctic areas with low but dense vegetation. snow depth variations and the challenges of RGB-based photogrammetry in vegetated terrain, we employ UAS LiDAR to generate high-resolution snow depth models. Its ability to capture vegetation and provide precise elevation data makes it particularly suitable for monitoring snow depth in subarctic permafrost landscapes.

Another method to estimate snow distribution is the application of statistical machine learning models like the *Random Forest* (RF) algorithm (Breiman, 2001), which — in snow research — has so far mainly been used. RF is a widely used method of ensemble learning that is characterized by complex, non-linear relationships between predictor variables and is therefore suitable for environmental modeling. In snow research, RF has been used primarily for large-scale mapping of snow distribution in mountainous regions (Meloche et al., 2022; Revuelto et al., 2020; Richiardi et al., 2023), where it has demonstrated good predictive capabilities through the integration of remote sensing, topographic and meteorological data. However, these studies have not been conducted at a small scale with very high resolution (\leq mainly focused on coarser spatial scales with resolutions of more than 1 m \times 1 m cell size), and — to our knowledge — no study has been conducted, which limits their applicability for analyzing small-scale snow distribution patterns. To our knowledge, RF has not yet been systematically applied to high-resolution snow depth modeling in subarctic and permafrost areas environments, such as Finnish Lapland.

As small-scale variations in snow depth play a crucial role in permafrost dynamics, investigating the feasibility of RF for such detailed applications could provide valuable insights for future research and monitoring needs.

130 In this study, we ~~applied a combination and comparison of all three mentioned methods by assessing~~ compare and evaluate
two methods for generating high-resolution snow distribution maps at three exemplary palsa sites in northernmost Finland:
~~i) precise snow depth data measured in the field; ii) snow distribution calculated with UAS data; and iii) simulated snow~~
~~distribution by a RF approach. The field~~ (i) snow depth derived from UAS LiDAR data and (ii) snow depth simulated using
a RF modeling approach. In-situ measured snow depth data was used to train the RF model as well as to validate the results
135 ~~given by remote sensing devices and models. The aim is to identify the most promising approaches for accurately determining~~
obtained with both methods. The primary objective of this study is to assess the accuracy and suitability of these methods
for small-scale snow distribution ~~and to test a method for generating precise snow distribution maps~~ mapping. Specifically,
~~this study evaluates whether machine learning~~ we investigate whether RF can effectively model small-scale snow ~~distribution;~~
~~providing snow researchers with depth patterns, providing~~ a cost-effective alternative to ~~expensive UAS-based methods~~ for
140 ~~future research. Furthermore, we provide a detailed assessment about the~~ UAS LiDAR methods. In addition, we investigate
the spatial distribution of snow depth at palsas and their ~~surrounding areas at a small scale. Therefore, this paper aims to~~
~~answer surroundings based on the results of the methods to identify characteristic small-scale variation patterns. The results~~
provide a basis for discussing relationships between snow distribution and palsa dynamics. To address these objectives, we
focus on the following research questions: ~~How is snow depth distributed at palsas at a small scale and is it possible to identify~~
145 ~~warming and cooling spots based on the results (1) and how accurate are snow distribution analyses based on UAS data and~~
~~the RF algorithm~~ How accurately can UAS LiDAR and RF modeling estimate snow depth, and which ~~are the most suitable~~
~~input parameter for the modeling approach~~ approach provides the most reliable results, (2) and how do the snow depth patterns
derived from UAS LiDAR and RF modeling compare, and what does this reveal about small-scale snow distribution?

~~The obtained results provide novel insights of precise snow distribution in palsa mires including knowledge about warming~~
150 ~~and cooling spots and its negative and positive effects. Furthermore, this information can improve our understanding of the~~
~~paradoxical effects of changing snow distribution due to global warming on the palsas.~~

2 Study sites

The palsa sites under investigation - Puolikkoniva, Pousu and Peera - are located ca. 30 km south from the closest Finnish
Meteorological Institute's (FMI) weather station in Kilpisjärvi, Finland (Fig. 1). These sites are located along the Könkämäeno
155 river, a significant terrain depression with numerous palsas, and are adjacent to the region's primary main road (European
Route E8) in the northwestern part of Finnish Lapland (Fig. 1 (a, b)). While Peera has been previously described by Verdonen
et al. (2023), Pousu and Puolikkoniva were not yet investigated.

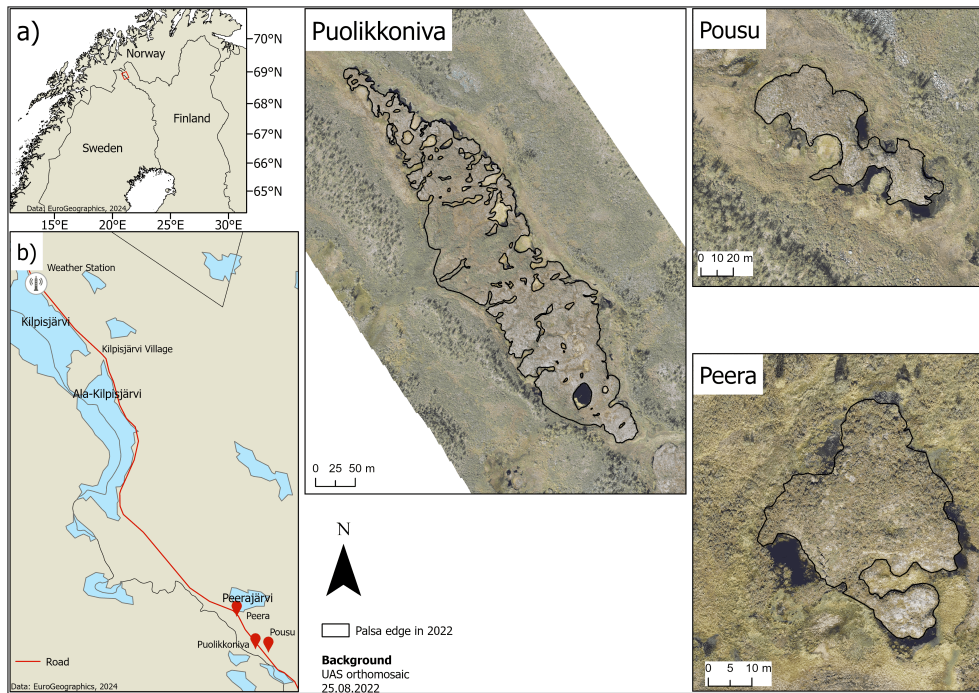


Figure 1. Location of the study sites Puolikkoniva, Pousu and Peera in north-western Finland (a). Climate data used in this study are from the Kilpisjärvi weather station, from which the distance to the palsa sites is around 20 km (b). Basemaps obtained from EuroGeographics (2024).

2.1 Palsa mire sites

Puolikkoniva is located approximately 2.3 km south of lake Peerajärvi at 68°51'43" N, 21°06'18" E and around 455 m a.s.l., surrounded at the eastern part by the ~~Peerasuvanto~~ Könkämäeno river and in the west by the main road. The study site has an area of roughly 4.26 ha with a maximum height difference to the surrounding peatland of ca. 2 m. This palsa is about 590 m in length and 130 m in width. Puolikkoniva is ~~the largest study site and~~ a prototypical longitudinal plateau palsa, consisting of several single and complex shaped palsas. According to the definition of Seppälä (2006) and Meier (2015), the palsas contain a perennially frozen core of peat with segregated ice. Numerous cracks traverse the palsa site, with dwarf shrubs (5 - 20 cm high, e.g. *Rubus chamaemorus*, *Empetrum hermaphroditum*) and ~~birches~~ dwarf birches (5 - 60 cm high, *Betula nana*) at the edges, while atop and around the palsas, typical vegetation such as lichens (up to 3 cm high, e.g. *Cetraria* spp., *Cladonia* spp.) and sphagnum ~~moss~~ (mosses (under 3 cm high, e.g. *Sphagnum lindbergii*) flourishes dominates). The absence of distinct dome-shaped structures and the presence of thermokarst ponds within the palsa structure indicate the degradation of the palsa (Seppälä, 2011), with pronounced block erosion at steep edges.

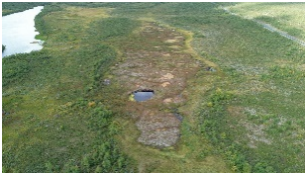


Pousu is located approximately 600 m east of the Puolikkoniva palsa at 68°51'39" N, 21°07'17" E and around 470 m a.s.l., 150 m east of the main road. This study site covers an area of about 0.36 ha and has a maximum height difference to the surrounding peatland of ca. 2.5 m. This site, measuring 130 m in length and 50 m in width, is a classic example of a degrading

dome-shaped palsa, as shown by collapsed parts, block erosion at its steep edges and thermokarst ponds within the former palsa structure. Similar to Puolikkoniva, typical palsa mire vegetation grows around and on it.

175 **Peera** is located at 68°52'45" N, 21°04'35" E and around 460 m a.s.l., approximately 400 m south of lake Peerajärvi and 100 m west of the main road. This study site encompasses an area of about 0.13 ha and has a maximum height difference to the surrounding peatland of ca. 2 m. This palsa is about 55 m in length and 45 m in width. The palsa structure is surrounded by typical peatland vegetation such as sphagnum mosses [and sedges](#). Water bodies, peat and bare rock structures can be found at the edges of the palsa. Mainly lichens and dwarf shrubs grow on top of the palsa. Similar to Pousu, this palsa is also dome-

180 shaped and in a degrading phase. ~~(Verdonen et al., 2023)~~ [Verdonen et al. \(2023\)](#) point out a ~~massive loss of the permafrost area~~ [significant decrease in the surface area of the palsa](#) during the past 15 to 60 years.

Table 1. Main characteristics of each palsa site. Images recorded with DJI mini 3 Pro UAS at 30.08.2023.

	Puolikkoniva	Pousu	Peera
UAS image			
Location	68°51'43" N, 21°06'18" E	68°51'39" N, 21°07'17" E	68°52'45" N, 21°04'35" E
Area	4.26 ha	0.36 ha	0.13 ha
Extent (length, width)	590 m, 130 m	130 m, 50 m	55 m, 45 m
Height	2 m	2.5 m	2 m

2.2 Climate

The investigation areas are located on the pre-alpine belt of the Scandes. For the time period ~~1990-1991~~ [1991](#) - 2020, the annual mean temperature is ~~-1.38~~ [-1.30](#) °C, the annual mean precipitation amount is about ~~514~~ [515](#) mm and the dominating wind direction is south-southeast from November to April (FMI, 2022). Higher mountains ~~affect the influence~~ [local weather conditions](#), ~~clouds for instance remain e.g. clouds get held~~ in front of ~~the mountain mountains~~ or wind directions are influenced (Autio and Heikkinen, 2002). This may lead to different precipitation amounts or wind directions and speeds than measured at the Kilpisjärvi weather station (Verdonen et al., 2023). Also, high wind speeds during winter can lead to a more intensive snow drift, influencing the snow ~~depth~~ distribution inside the mire sites (DeWalle and Rango, 2008).

190 The palsa mire sites are affected by cold winters and moderate warm summers (Fig. 2). Winter is the longest season, lasting about 200 days including the polar night with around 50 days without sunlight. During winter the temperature can drop close to - 50 °C and can increase above 0 °C (FMI, 2024). In Kilpisjärvi, the duration of permanent snow cover lasts about 217 days a year (Lépy and Pasanen, 2017). During spring, the snow cover melts away, and the growing season starts in late May. In late August the growing season ends with the beginning of autumn which lasts around 102 days (Kauhanen, 2013).

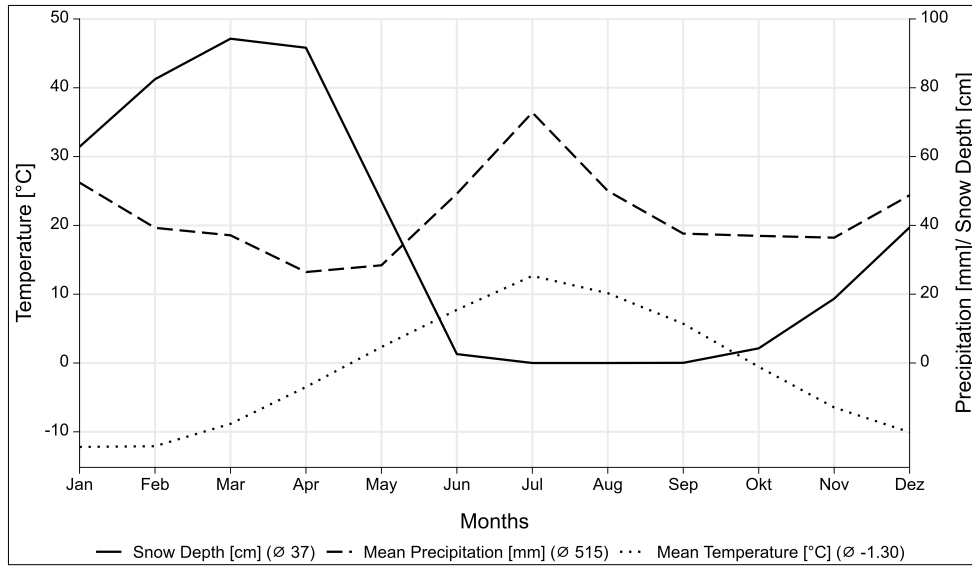


Figure 2. Climate chart of Kilpisjärvi (FMI, 2022). [Climate data measured at 69.03905N, 20.81379E and 474 m.a.s.l. in the period 1991 - 2020.](#) Dotted line shows 2 m above ground temperature in °C, dashed line shows precipitation in mm and solid line shows snow depth in cm. [The Köppen-Geiger climate classification is Dfc.](#)

195 3 Data and methods

In [late](#) August 2022 and [late](#) March 2023, field expeditions to the palsa mire sites were conducted to collect a comprehensive dataset. ~~The selection of August for the summer dataset collection was strategic, corresponding consisting of UAS LiDAR data and in-situ snow depth measurements for modeling purposes.~~ [Late August was chosen specifically for the collection of summer data as it corresponds with the peak of the growing season and the maximum ALT, which typically occurs in this region by the end of August and mid-September, depending on annual weather patterns and the onset of frost](#) (Verdonen et al., 2003). This timing ensures the capture of the landscape's conditions in its ~~most diverse various~~ states before the start of the winter season, providing the basis for extracting relevant input parameters for our approach. [The input parameters are spatial datasets calculated on the basis of elevation data derived from UAS LiDAR.](#)

On the contrary, ~~the winter dataset, collected in March 2023, was chosen~~ [late March was chosen for the the winter dataset](#) based on historical climatological patterns in the Kilpisjärvi region, which typically have maximum snow depths at this time (FMI, 2024). This period ~~allows-allowed~~ the collection of data under conditions that reflect winter extremes, which serves as both validation and training data for the RF modeling. Figure 3 shows an overview of the different steps carried out for this work.

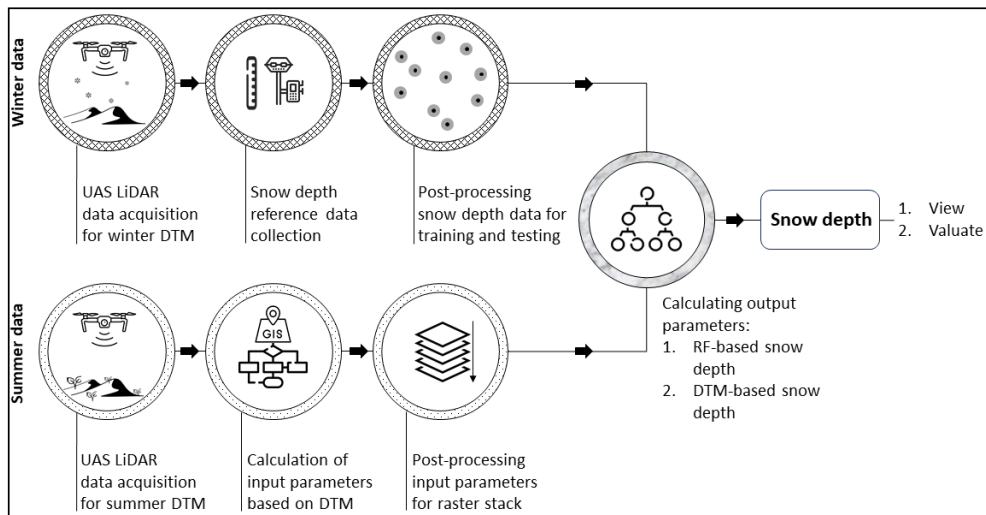


Figure 3. General overview of the data collection and analysis.

3.1 UAS Data collection ~~For the collection of input parameter data-~~

210 3.1.1 UAS data collection

For the initial collection of UAS LiDAR data to generate input parameters, aerial surveys were conducted at all three study sites ~~during summer on August 27, 2022~~, using a DJI Matrice 300 RTK, equipped with a YellowScan Mapper+ LiDAR system that scanned at a wavelength of 905 nm. The flight altitude was 30 m for each palsa, with a 50% side overlap. The flight direction was along the longitudinal axis of the palsas, except for Peera palsa, which followed an east-west orientation. The flight trajectories are pictured in Fig. 4. To improve the accuracy of the collected data, we used Ground Control Points (GCPs) ~~were set using~~, measured with a Trimble R12i Real-Time Kinematic (RTK) GNSS. We have established several permanent GCPs located on known points of large stones in the study sites. Permanent GCPs have been established because we are monitoring changes in the palsas by collecting drone data annually since the past 8 years. The accuracy of these RTK GPS-measured GCPs is between 1–2 cm. For all UAS LiDAR summer flights we utilized these GCPs: three for Peera, 20 for Pousu, and 30 for Puolikkoniva.

The winter survey replicated the methodological framework of the summer survey, using the same drone and sensor. The flights for all three study sites were carried out on March 23 (Puolikkoniva and Pousu) and 24 (Peera), 2023. The flight altitude was 60 m, with a 50% side overlap. The flight direction was along the longitudinal axis of each palsa (see Fig. 4). For each side we used four GCPs, positioned around the palsa. The accuracy for each GCP is between 1 - 2 cm.

225 In addition, ~~with the integrated high-resolution RGB sensor of the DJI Matrice 300 RTK, images were captured, RGB images were captured with an Autel EVO II Pro V2 to create an orthopicture in Agisoft Metashape Professional software of each palsa site during both surveys, enabling a comprehensive analysis of the sites' conditions, the site's conditions. The flight altitude was 80 m, with a 75% side overlap for each flight. The RGB flights were conducted using the drone's internal RTK system.~~

3.1.2 UAS data post-processing

230 ~~These aerial missions were post-processed in detail using YellowScan CloudStation Agisoft Metashape Professional Software, resulting in Digital Surface Models (DSMs) with a raster cell resolution of 0.1 m x 0.1 m. No additional filtering or noise removal was performed on the UAS LiDAR data, keeping vegetation in the DSMs. Structure from Motion techniques were not applied and no imagery was used in the post-processing. Orthophotos were also created to provide detailed visual representations of the terrain.~~ The acquired LiDAR data were post-processed using YellowScan CloudStation, resulting in point clouds for each
235 ~~flight.~~ Mean point ~~cloud densities per raster cell vary from 7.2~~ densities per square meter vary from 1064 (summer) to 91
831 (winter) for Peera site, ~~9.9 to 8.1~~ four 308 to 338 for Pousu site and ~~6.6 to 9.0~~ 260 to 313 for Puolikkoniva site. To
refine the flight trajectories, we used Receiver Independent Exchange Format (RINEX) data in the Position and Orientation
System Post-processing software (POSPac). For each dataset, we obtained RINEX data from the continuously operating
reference station (CORS) of the National Land Survey of Finland (NLS) in Kilpisjärvi (*KILP 2147250.4266 820562.0462*
240 *5930136.8831*).
~~The winter survey replicated the methodological framework of the summer survey, using the same UAS and sensor configurations to produce DSMs and orthophotos. For noise and vegetation removal in the dataset, we used the progressive Morphological Filter (PMF) described by (Zhang et al., 2003) and (Jacobs et al., 2021) in order to receive Digital Terrain Models (DTM). We applied the filtering using window sizes of 0.5, 1, 2 and 3 and thresholds of 0.05, 0.1, 0.3 and 0.5. The extracted ground points~~
245 ~~were saved in point cloud format. Using the software CloudCompare, we generated a DTM for each flight mission in 0.1 m x 0.1 m resolution with the Rasterize function. Empty cells within the point clouds were interpolated with a triangle max edge length value of 5.0.~~
Based on the summer and winter ~~DSM-DTM~~ of the palsa sites, snow distribution datasets were calculated by subtracting the
winter by the summer ~~DSM-DTM~~ in Geographic Information Systems (GIS) - *ArcGIS Pro* by Esri was used -, allowing the
250 comparison of ~~UAS-LiDAR~~ UAS LiDAR conducted snow depth (SD_{LiDAR}) and RF modeled (SD_{RF}).

3.2 Reference data collection

Additional datasets that are essential for modeling and validation were collected after the respective flights. Snow depth measurements ($SD_{in-situ}$) were carried out manually using a wooden yardstick across all sites, whereas each point was measured ~~by~~
~~RTK-GPS.~~ at the snow cover surface by RTK GPS to receive the exact location. On March 23, 2023, $SD_{in-situ}$ were measured
255 in Puolikkoniva and Pousu and on March 24, 2023, in Peera. A total of 185 validation points were recorded, divided across the
sites as follows: 100 in Puolikkoniva, 46 in Pousu, and 39 in Peera (Fig. 4).
To ensure the derivation of ~~an optimal~~ a diverse $SD_{in-situ}$ training dataset, different measurement network designs were at-
tempted at each site, customised to the unique geomorphological features of the palsa mires, making sure to catch points on
top of the palsa, at the edges and at the steep slopes, on the thermokarst ponds and the surrounding field as at those parts
260 differences in snow depth can be expected. In Pousu, a randomised sampling strategy was applied with focus on the palsa
edges and summits (Fig. 4 b). In Puolikkoniva, there were two parallel transects measured following its longitude shape and

complemented by randomised points at the edge, thermokarst and surrounding field (Fig. 4 a). The Peera approach consisted of two intersecting transects, augmented by a set of randomly chosen points along the edge (Fig. 4 c). This training dataset captures the variability of snow cover within palsa mires, ranging from snow-free palsa summits to deeply covered palsa edges, allowing a distribution of all $SD_{in-situ}$ into point classes *Edge*, *On Top*, *Open Area* and *Thermokarst*. A histogram of the snow measurements $SD_{in-situ}$ can be viewed in Appendix A1 and the distribution to the respective classes in Appendix A2.

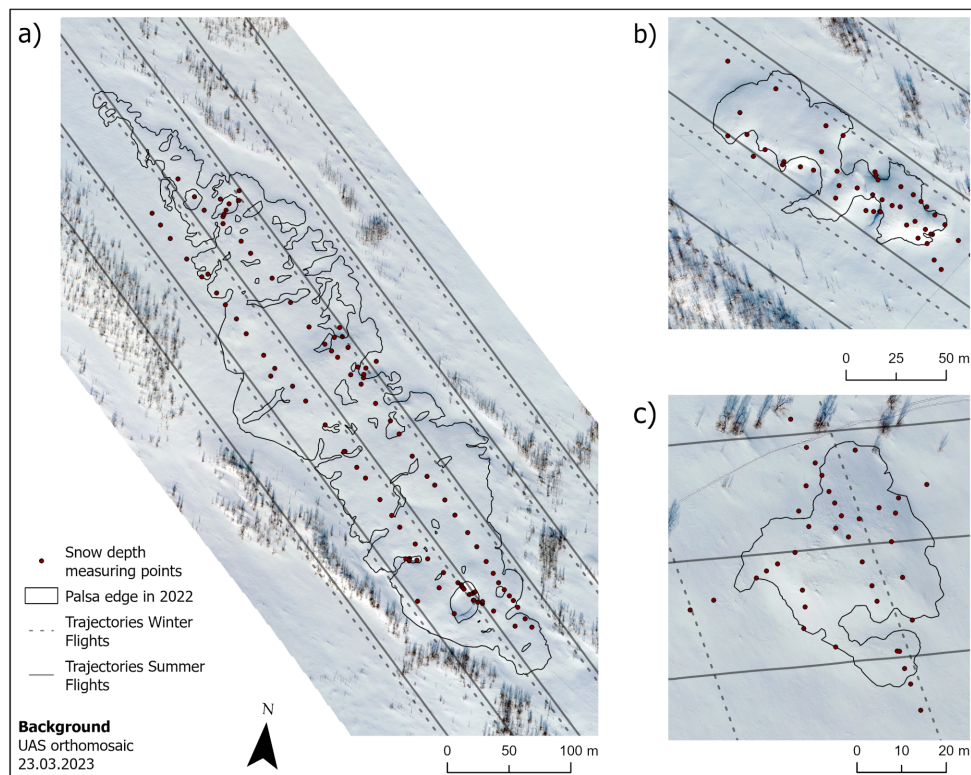


Figure 4. Snow depth measuring points within the investigation sites at Puolikkoniva (a), Pousu (b) and Peera (c) palsa illustrating different methods for recording snow depth (transects, randomized, crossed).

3.3 Random Forest algorithm Modeling data preparation

For the modeling process, we used The collected LiDAR data from the summer flight missions were used to create the input parameters for the **ranger** package (Wright and Zigler, 2017) within the R programming environment, which is known for its ability to efficiently process large datasets and accounts for complicated predictor interactions. The preparatory steps included aggregating the various input parameters into a uniform raster stack, conducted by the *stack* function from the **raster** package (Hijmans et al., 2023). This method allowed for a comprehensive analysis of the multidimensional dataset, ensuring spatial alignment across all layers.

275 The dependent variable for our model was the previous-described $SD_{in-situ}$ dataset. These measurements, together with the stacked input parameters (Table 2) as independent variables, formed the basis of our RF model. The process of extracting input parameter values from the stacked raster set was performed using the buffered shapefile. This procedure was crucial for the preparation of the training dataset, which was subsequently split randomly into training (70%) and testing (30%) subsets for all palsa locations combined. This split allowed an evaluation of the model's predictive accuracy.

280 The RF model was used without explicit hyperparameter specifications, so default settings were used, including the construction of 500 decision trees, a maximum of 3 variables per split, and a target node size of 5, reflecting the characteristics of the final model run (12 input parameters). Permutation mode was chosen for variable importance assessment, and a specific seed value was implemented to ensure reproducibility of the results. The resulting Permutation Importance (PI) value of each input parameter was given and—for better understanding and comparability—the PI values were converted into percentages over all input parameters. Subsequently, the trained RF model was employed to calculate SD_{RF} predictions across each palsa site. For 285 that, the *predict* function was used, applying the model to the test dataset to estimate snow depth values.

3.4 Modeling data preparation

The collected airborne data were subjected to extensive preprocessing using GIS, in particular *ArcGIS Pro* and RF modeling in SAGA GIS by SourceForge. This preprocessing aimed to match the datasets (cell size 0.1 m x 0.1 m) by SourceForge. For that, we used the created DTMs as input for the creation of all parameters and afterwards resampled these raster to the same extent 290 and resolution in ArcGIS Pro, making it suitable for analysis with the RF algorithm.

Subsequently, *SAGA GIS* was used for the computation of various geomorphological parameters to enhance the training dataset with a diverse range of topographical and environmental predictors. These predictors included elevation, aspect, slope, and a range of indices comprising hydrological and morphological landscape features (Table 2). According to Meloche et al. (2022) and Revuelto et al. (2020), the *Topographic Position Index* (TPI) is most suitable of great relevance when modeling snow 295 distributions due to its proven relevance to show importance for representing dependencies between topography and snow depth.

To reduce the risk of possible overfitting, the *Elevation* parameter was purposely excluded in the subsequent model iteration. Further refinement was based on the RF algorithm's PI values, leading to the exclusion of parameters with initial minimal impact on model performance ($PI < 1.25\%$) for the final model iteration. These parameters included: *Analytical Hillshading*, 300 *Convergence Index*, *LS Factor*, *Plan Curvature*, *Profile Curvature*, *Real Surface Area*, *Terrain Ruggedness Index*, *Topographic Wetness Index*, and *Total Catchment Area* (see Table 2).

The $SD_{in-situ}$ locations, serving as the training dataset, were buffered by 0.3 m, with each buffered point assigned the corresponding snow depth value. This buffering strategy aimed to moderate model variability and offers a balanced representation of parameter combinations linked to the specific $SD_{in-situ}$ measurements, improving the realism and consistency of the model 305 as proven in Bergamo et al. (2023).

Table 2. Overview of all input parameter used in the RF modeling.

Parameter	Description
Analytical Hillshading Parameter shows landscape as shaded by the sunlight from a specific direction (Tarini et al., 2006). Inserts topographical structures to the training data set. <i>Aspect</i>	Aspect in degree of every raster cell (Olaya, 2009).
<i>Channel Network Base Level</i>	Gives information <u>Provides information about</u> channel networks and interpolates the base level elevations of it (Olaya and Conrad, 2009).
<i>Channel Network Distance</i>	Gives information about the vertical distance from altitudes above the channel network to its base (Olaya and Conrad, 2009).
Convergence Index Shows an index of convergence in relation to the overland flow (Kiss, 2004). <i>Elevation</i>	The elevation calculated from remote sensing data in Agisoft Metashape Professional.
LS Factor The factorised length and steepness of a slope (Böhner and Selige, 2006) Negative Openness	Parameter which indicates how enclosed the location of a landscape is (Yokoyama et al., 2002).
Plan Curvature Describes the curvature of the surface, with positive values indicating areas of convergent and negative values divergent flow (Wood, 1996). <i>Positive</i> <i>Openness</i>	Parameter which indicates how dominant the location of a landscape is (Yokoyama et al., 2002).
Profile Curvature Describes the curvature where the Z-axis intersects with the direction of maximum gradient, with positive values indicating convex and negative values concave profile. (Wood, 1996). <i>Real</i>	<u>Providing</u> <u>Provides</u> a measure of each cell's position in relation to the surrounding terrain (Böhner and Selige, 2006).

3.4 Random Forest algorithm

For the modeling process, we used the **ranger** package (Wright and Zigler, 2017) within the R programming environment, which is known for its ability to efficiently process large datasets and accounts for complicated predictor interactions. The preparatory steps included aggregating the various input parameters into a uniform raster stack, conducted by the *stack* function from the **raster** package (Hijmans et al., 2023), ensuring spatial alignment across all layers.

The dependent variable for our model was the previously described $SD_{in-situ}$. These measurements, together with the stacked input parameters (Table 2) as independent variables, formed the basis of our RF model. The $SD_{in-situ}$ locations, serving as the training dataset, were buffered by 0.3 m, with each buffered point assigned to the corresponding snow depth value. The process of extracting input parameter values from the stacked raster set was performed by randomly separating 70% of the point features from each $SD_{in-situ}$ dataset for training and 30% for testing. After this separation we extracted the input parameter values for the training dataset, ensuring a clear distinction between training and testing data. The input parameters were not averaged within the buffer areas; instead, each parameter value was directly linked to the respective $SD_{in-situ}$ measurement. Consequently, each snow depth value is associated with an average of 28 input parameter values, leading to a dataset consisting of 3645 training values (Puolikkoniva 1983; Pousu 905; Peera 757) and 1577 test values (836; 401; 340). The buffering strategy aimed to moderate model variability, reduce noise, minimize the influence of geolocation and sampling errors, and enhance the robustness of the model by increasing the number of training points. By incorporating groupings of nearby points rather than relying on single-point measurements, this approach helps improve the model's stability and realism, as demonstrated in Bergamo et al. (2023). To prevent errors and miscalculations, all *NoData* values were removed from the datasets, resulting in a final training dataset of 3504 points and a final test dataset of 1548 points for further modeling and validation.

To determine the optimal values for *mtry*, *min.node.size*, and *sample fraction*, we performed hyperparameter tuning using the **mlr** package in R (Bischl et al., 2016). To prevent overfitting, we restricted the search range for *min.node.size* to 10–15 and for *sample fraction* to 0.7–0.85, following the recommendations of Probst et al. (2019) and Breiman (2001). Allowing an unlimited search range initially resulted in better model performance, but at the cost of reduced generalization, indicating signs of overfitting. We selected the final search range based on multiple test runs with different settings. For cross-validation, we tested different fold sizes to identify the most effective configuration. The best results were achieved using a 4-fold cross-validation. The final tuned hyperparameters values were as follows: *mtry*: 9; *min.node.size*: 10; *sample fraction*: 0.79.

Permutation mode was chosen for variable importance assessment, and a specific seed value was implemented to ensure reproducibility of the results. For more robustness, we repeated the calculation 100 times to obtain a mean permutation importance (PI) value for each input parameter, ensuring reliable rankings. The resulting PI values for each input parameter were normalized for better comparison by setting the most important parameter to 1. Subsequently, the trained RF model was employed to calculate SD_{RF} predictions across each palsa site by using the *predict* function.

Additionally, a correlation analysis between the input parameters and predicted SD_{RF} was performed to identify any correlating predictors and assess the strength of the relationships between them and the prediction. Correlation values for all input parameter are listed in Appendix A3. Furthermore, the RF model was run three additional times to ensure a fully external

340 validation. In each run, one palisa site was excluded from the training data, allowing its measured $SD_{in-situ}$ values to be used exclusively for validation.

3.5 Statistical analysis

The statistical analysis focused on evaluating the predictive accuracy of the model. The following metrics were summarized for all palisa sites and calculated in the R environment:

- 345 1. **Coefficient of Determination (R^2):** Calculated to quantify the proportion of variance in the dependent variable that is predictable from the independent variables in the model (Nagelkerke, 1991), giving clearance about the overall effectiveness of the model, defined as

$$R^2 = 1 - \frac{\sum (y_i - \hat{y}_i)^2}{\sum (y_i - \bar{y})^2} \quad (1)$$

- 350 2. **Root Mean Square Error (RMSE):** Employed to quantify the average magnitude of the error in the predictions (Chai and Draxler, 2014), highlighting the ability of the model to predict snow depth accurately, defined as

$$RMSE = \sqrt{\frac{1}{n} \sum (y_i - \hat{y}_i)^2} \quad (2)$$

3. **Mean Absolute Error (MAE):** Measures the average magnitude of the absolute errors between predicted and observed values, without considering their direction (Chai and Draxler, 2014; Willmott and Matsuura, 2005), defined as

$$MAE = \frac{1}{n} \sum_{i=1}^n |y_i - \hat{y}_i| \quad (3)$$

- 355 4. **Standard Deviation (SD):** Provides a measure of the dispersion of prediction errors around their mean (Walser, 2011), revealing the precision and consistency of the predictions, defined as

$$SD = \sqrt{\frac{1}{n-1} \sum_{i=1}^n (y_i - \hat{y}_i)^2} \quad (4)$$

where y_i is the observed value, \hat{y}_i is the predicted value from the model, \bar{y} is the mean of observed values.

~~Furthermore a 10-fold cross-validation according to James et al. (2013) was done in RStudio using the **caret** package (Kuhn, 2008) to further validate the model and mitigate the risk of overfitting. This method divides the $SD_{in-situ}$ training data into ten subsets, trains the model on 9 subsets, and evaluates it on the remaining one. This cycle was repeated ten times, with each subset serving as the test set once, ensuring that every data point is used for both training and testing. The choice of 10 folds balances the need for model evaluation with computational efficiency. In the end, the mean R^2 and RMSE were calculated, allowing the comparison with the initially calculated values.~~

365 ~~Additionally, a correlation analysis between the input parameters and predicted SD_{RF} was performed to identify any significant predictors and assess their influence on the model's predictions. Special focus was set to parameters exceeding or fall below a correlation of ± 0.7 , indicating a significant influence on the model performance.~~

To visualize the statistical analysis results, scatter plots ~~of~~ were created to compare RF and UAS LiDAR derived snow depths ~~in comparison to the measured values~~ were conducted with the test dataset values.

370 4 Results

4.1 Snow depth predictions

~~The~~ In general, the predicted SD_{RF} present a good visual alignment with the calculated SD_{LiDAR} (Fig. 5).

The **Puolikkoniva** palsa site is affected by several collapsed areas, in which snow accumulates ~~massively~~ heavily. This can be seen in the SD_{RF} (Fig. 5 a) as well as in the SD_{LiDAR} (Fig. 5 b) results. ~~In general, the~~ At the eastern side of the palsa, RF models
375 the snow depth inside these collapsed holes and cracks ~~slightly~~ higher than the UAS LiDAR was detecting it. Especially directly at the steep edges of the palsa, the depth values increase up to ~~30 cm~~ 20 - 40 cm, partly up to 60 cm. At the western side of the palsa, SD_{LiDAR} is higher at these parts with values increasing up to 20 - 40 cm compared to SD_{RF} . However, the transition of the snow depths better corresponds to changes at slopes on the UAS LiDAR results, as the RF model reveals obvious patterns. The most obvious differences are occurring in areas beneath the palsa itself, for example the whole northeastern and eastern
380 parts directly at the edge of the palsa, which have higher snow depths (up to 60 cm) predicted by RF than detected based on the UAS LiDAR data. Within the open area beneath the palsa, SD_{LiDAR} is higher (up to 50 cm), following areas with higher vegetation. The most similar parts are the areas on top of the palsa with ~~slightly higher snow depths predicted by RF~~ differences between both datasets under 15 cm, partly 20 cm.

The **Pousu** palsa site shows a similar pattern as in the Puolikkoniva palsa site, with cracks filled by snow and collapsed parts
385 with steep slopes where snow accumulated heavily (Fig. 5 c, d). Again, the transition of the snow depth at those areas is more natural in the SD_{LiDAR} data since the SD_{RF} data are showing sharp steps. Also, mire areas ~~parts~~ next to the palsa are observed by UAS LiDAR with lower snow depth as modeled with RF. This is especially visible in the southwestern and southern parts of the area, where snow ~~height~~ depth was modeled between 40 – 50 cm and the UAS LiDAR detected values between 10 – 20 cm. However, similarities are visible on top of the palsa, where snow depths were modeled and observed in a range between
390 10 to 30 cm each.

The **Peera** palsa site shows the highest consistency between SD_{RF} and SD_{LiDAR} . However, as in the two former sites, the highest snow ~~pack~~ depth accumulated in cracks and at the steep edges of the palsa (Fig. 5 e, f). Unlike at the other locations, there are no sharp steps at the parts mentioned here, as both approaches model smooth transitions. Similar structures are also visible on top of the palsa with snow ~~heights~~ depths around 20 cm in each approach. However, differences are visible like at the two other
395 palsa sites in the surrounding area of the palsa, where the snow ~~pack~~ depth is calculated higher by RF than the UAS LiDAR detected it. Higher snow depths were also calculated with RF on the northwestern edge of the Palsa than measured with LiDAR (up to 30-50 cm).

~~Snow depth predictions based on the RF model run 3 (left) and the UAS LiDAR (right) at site Puolikkoniva (a, b), Pousu (c, d) and Peera (e, f) palsas. Red points are showing the in-situ snow depth measurement locations:~~

400 ~~Snow depth differences between modeled and UAS LiDAR results at a) Puolikkoniva, b) Pousu and c) Peera palsas.~~

Viewing the deviations in snow ~~height~~depth between the two approaches, it is evident that the top parts of the palsa sites themselves show very low differences (Fig. 6 a, b, c). However, deviations occurred at the edges, inside of cracks, at the highest parts of the palsa and in the surrounding areas. Within cracks on top of the palsa sites, the UAS LiDAR detected in general higher snow ~~paek~~depth than RF modeled it, except for the eastern side of Puolikkoniva palsa, where it is the other way
405 around. Differences of around 20 cm are shown, but with peaks up to ~~50-60~~ cm. Also, highest elevated structures of the palsa sites directly at edges show deviations of about 15 - ~~30-40~~ cm higher snow ~~paek~~depth calculated by the UAS LiDAR, except for Peera palsa. In contrast, the collapsed parts with accumulated snow are consistently modeled with higher values exceeding 45 cm of deviation to the UAS LiDAR derived values. ~~It is worth noting that the~~ Notably, deviations in the areas surrounding the palsas are ~~mostly in the type of higher modeled snow from~~ primarily characterized by higher snow depths predicted by the
410 RF model ~~.Only a few narrow structures with significantly higher snow can be recognized based on the UAS LiDAR data~~ with exception for areas with higher vegetation at Puolikkoniva palsa site.

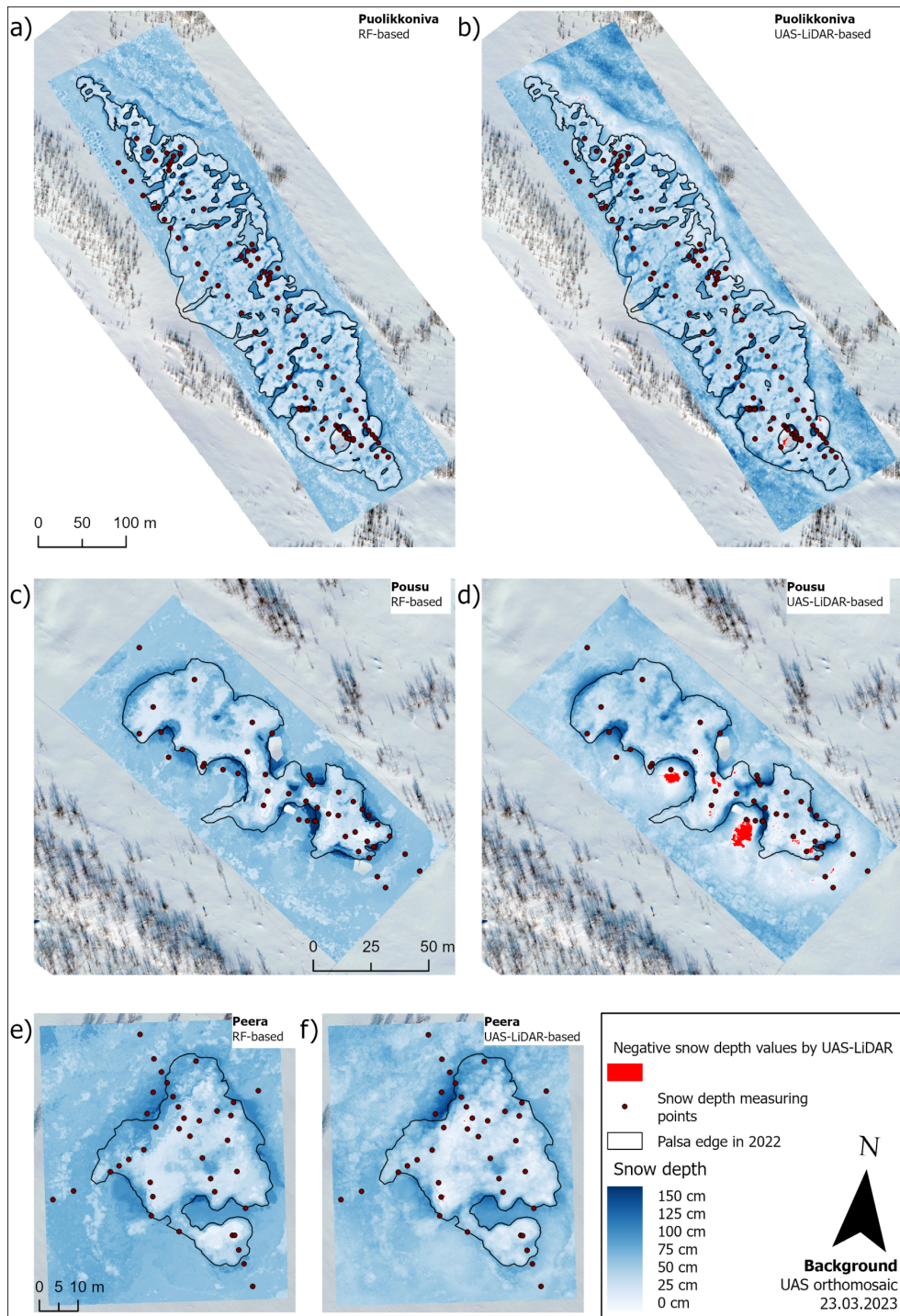


Figure 5. Snow depth predictions based on the RF model (left) and the UAS LiDAR (right) at site Puolikkoniva (a, b), Pousu (c, d) and Peera (e, f) palsas. Red points are showing $SD_{in-situ}$ locations.

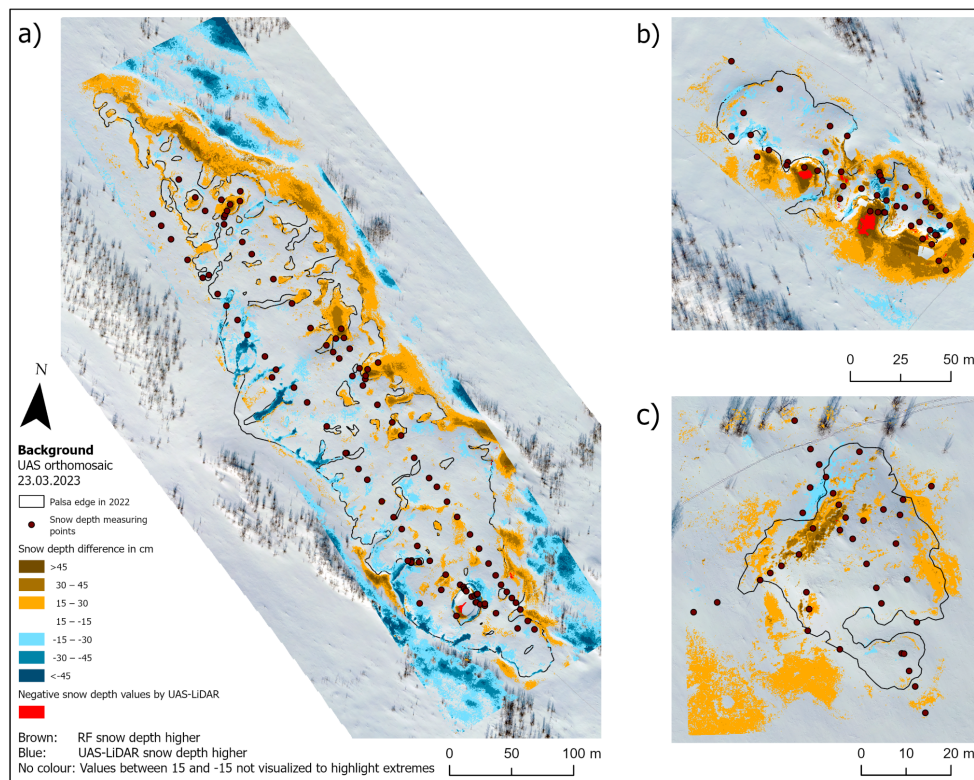


Figure 6. Snow depth differences between modeled and UAS LiDAR results at a) Puolikkoniva, b) Pousu and c) Peera palsas.

4.2 Variable ~~importance~~importance

The calculated PI ~~shares values~~ of all parameters ~~for all model runs~~ are pictured in Fig. 7. ~~In model run 1, the~~ The four most important parameters are *TPI*, *Wind Effect*Exposition, *Valley Depth*Elevation and *Channel Network Base Level*, while *TPI* is
 415 ~~nearly three times more important (29.36 %) than the second~~ the most important parameter ~~with 9.33 %~~. Low importances are shown for the parameters *Terrain Ruggedness Index*, *Real Surface Area*, *Analytical Hillshading*, *Profile Curvature*, *Topographic Wetness Index*, *LS Factor*, *Total Catchment Area*, *Plan Curvature* and *Convergence Index*. These parameters showed a PI-value lower than 1.25 %, which is about 24 times less than the most important parameter *TPI*.

After removing the parameter *Elevation* for model run 2 and all parameters with PI-values lower than 1.25 % for model
 420 ~~run 3, slight changes in PI values can be recognized. The remove of~~ and set to 1. It is more than four times more important
~~than the two following parameters~~ ElevationWind Exposition led to a minor PI-value increase for 15 parameters and slight decrease for 5 parameters. However, removing all parameters with PI-values lower than 1.25 % increased the importance of all remaining parameters, especially for the four most important parameters and ~~(around 0.14)~~ Elevation (0.13). In addition, *Channel Network Base Level* (0.12), *Wind Effect* (0.08) and *Elevation*valley Depth as well as *Wind Exposition* with 8–15 %

total-increase- (0.07) are also of substantial importance. The remaining input parameter *Positive Openness*, *Channel Network Distance*, *Relative Slope Position*, *Negative Openness*, *Slope*, *Aspect* possess lower importance than 0.04.

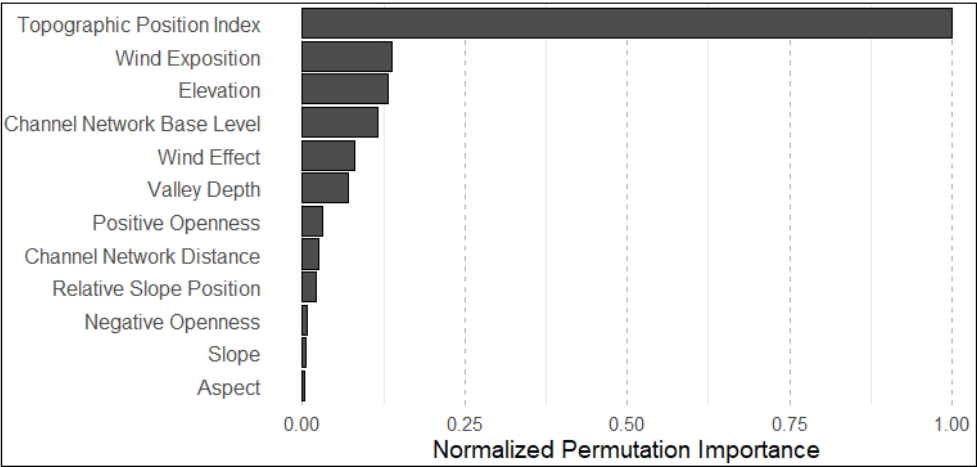


Figure 7. Overview of percentage shares of PI per input parameter and model run normalized mean Permutation Importance values from RF modeling over 100 iterations.

4.3 Statistical evaluation results

The statistical analysis by model run of the general (Table 3) and validation point locations accuracy (Table 4) reveals high precision-comparable high accuracy of SD_{RF} :-

While each model run has significantly better and SD_{LiDAR} . The RF modeling dataset has slightly better statistical validation metrics than the SD_{LiDAR} ; only minor differences are found between model runs. The RMSE amounts to 6.16 cm for model run 3, which is about 1.2 cm better than the worst model run 2. Same tendencies can be seen for dataset with a RMSE of 18.33 cm compared to 23.49 cm. Furthermore, R^2 , MAE and SD with model run 3 having the best and model run 2 the worst results among all. However, the SD_{LiDAR} results drop off in accuracy for each metric compared to the model runs with 20 cm worse RMSE are better in the RF modeling with values of 0.770, a R^2 13.26 cm and 18.11 cm compared to 0.691, 17.49 cm and 20.84 cm. The external validation results of the RF modeling dataset for each palsa (Table 3) indicate the best performance at the Peera site, with an RMSE of 16.67 cm and an R^2 of 0.59 and MAE respectively SD with ea. 15 cm and 19 cm higher values 0.628. At the Pousu site, the RMSE is higher (21.31 cm), but the R^2 improves to 0.767. The Puolikkoniva site shows the weakest performance, with both metrics being the lowest: an RMSE of 27.13 cm and an R^2 of 0.578.

Separated to When analysed by point groups, the results of SD_{RF} show clear trends among the individual groups. While RMSE, MAE and SD is in group RF and SD_{LiDAR} results show strong similarities for the *On Top* and *Edge* classes, while the *Thermokarst* and *Open Area* best (1.42 cm, 0.89 cm, 1.39 cm), followed by *Thermokarst* (1.44 cm, 0.98 cm, 1.42 cm), classes exhibit better metrics in the SD_{RF} dataset. RMSE and MAE values are identical for both datasets in the *On Top* (1.79 cm, 0.99 cm, 1.73 cm 8.33 cm, 3.84 cm) and *Edge* (2.56 cm, 1.44 cm, 2.55 cm), for metric R^2 there are no significant differences among

each-group (all 0.99). However, the same metrics – but for SD_{LiDAR} and SD_{LiDARRF} – were revealing significant differences. Each accuracy metric shows lower results compared to the RF performance, but also the order of point groups shows different results. Thus, group (On Top) contains the best RMSE and MAE (17.01 cm: 0.841, 12.20 cm) among the groups followed by Open Area (17.33 cm, 14.18 cm), Edge (32.53 cm, 22.66 cm) and Thermokarst (40.73 cm, 34.04 cm), but for: 0.894) compared to SD_{Open Area} is best (14.20 cm) followed by On Top (16.87 cm), Thermokarst_{LiDAR} (24.21 cm) and Edge (30.46 cm). The R² metric shows a completely different order with best results for Edge (0.48) followed by 0.730, 0.768). A similar trend is observed for standard deviation, with values of 8.32 cm versus 10.83 cm in the On Top class and 12.82 cm versus 19.09 cm in the Edge class. The Thermokarst (0.22) class consistently shows better metrics in SD_{RF} compared to SD_{LiDAR}, with RMSE of 10.99 cm compared to 33.73 cm, R² of 0.893 to 0.592, MAE of 5.42 cm to 30.35 cm and SD of 10.69 cm to 25.08 cm. A similar pattern is observed for the Open Area class, where RMSE improves from 14.23 cm (0.16) and On Top SD_{LiDAR} to 4.45 cm (0.00) SD_{RF}, R² from 0.519 to 0.926, MAE from 9.84 cm to 1.56 cm, and SD from 12.59 cm to 4.40 cm.

Table 3. Overview of the calculated Root Mean Square Error (RMSE) in cm, Coefficient of Determination (R²), Mean Absolute Error (MAE) in cm and Standard Deviation (SD) in cm for model runs 1 to 3 RF- and UAS LiDAR LiDAR-derived snow depth estimations. Additionally, external validation results (RMSE and R²) for RF-modeled snow depth at each palsa site (Peera RF, Pousu RF, Puolikkoniva RF) are provided.

Parameter	Model-Run-1RF	Model-Run-2LiDAR UAS	Model-Run-3Peera RF	UAS LiDAR Snow-DepthPousu RF	Puolikkoniva RF
RMSE	6.98-18.33	7.34-23.49	6.16-16.67	26.7321.31	27.13
R ²	0.97-0.770	0.97-0.691	0.98-0.628	0.590.767	0.578
MAE	4.39-13.26	4.59-17.49	3.25-	18.68-	-
SD	6.97-18.11	7.34-20.84	6.16-	25.15-	-

Table 4. Overview of RMSE in cm, R², MAE (cm) and SD (cm) divided by validation point locations within the investigation areas.

	RMSE		R ²		MAE		SD	
	RF	LiDAR	RF	LiDAR	RF	LiDAR	RF	LiDAR
On Top (n = 69)	1.79-8.33	17.01-8.33	0.995-0.841	0.009-0.730	0.99-3.84	12.20-3.84	1.73-8.32	16.87-10.83
Edge (n = 66)	2.56-13.12	32.53-13.12	0.996-0.894	0.482-0.768	1.44-5.85	22.66-5.85	2.55-12.82	30.46-19.09
Thermokarst (n = 16)	1.44-10.99	40.73-33.73	0.999-0.893	0.223-0.592	0.98-5.42	34.04-30.35	1.42-10.69	24.21-25.08
Open Area (n = 26)	1.42-4.54	17.33-14.23	0.993-0.926	0.163-0.519	0.89-1.56	14.18-9.84	1.39-4.40	14.20-12.59

The presented scatter plots of both approaches (Fig. 8) are revealing further insights into the accuracy of the results. On the left, the plot depicts the relationship between SD_{in-situ} and SD_{Both} SD_{LiDAR} and on the right, SD_{RF} results are compared to it.

The UAS LiDAR approach shows a positive linear relationship between detected and measured snow depths. However, variability is visible especially at higher snow depths. The RF approach shows a strong positive linear relationship with data points closely following the trend line and exhibiting minimal deviation, meaning a higher correlation between SD_{RF} and

465 ~~SD_{in-situ} than for SD~~(left plot) and ~~SD_{RF}~~ (right plot) show a positive correlation with the ~~SD_{in-situ}~~. The regression line in both plots closely follows the expected trend, showing that both methods capture snow depth patterns well. The ~~SD_{LiDAR} can be observed~~ have a tighter spread around the regression line, indicating lower variance compared to the ~~SD_{RF}~~. The spread of residuals (black dots deviating from the regression line) increases with snow depth in both cases, indicating larger uncertainty for deeper snow, while the confidence intervals remain narrow at lower snow depths. A single negative outlier is present for ~~SD_{LiDAR}~~.

Scatter plots with regression lines of the UAS LiDAR-derived and RF-modeled snow depths.

470 The 10-fold cross-validation supports the validation results shown above and, with an R^2 of 0.97 and an RMSE of 6.4 cm, shows good consistency with the statistical metrics mentioned above. In addition, the correlation analysis ~~of between~~ the input parameters and ~~SD_{RF}~~ shows a high correlation for the ~~reveals a strong negative correlation with~~ *TPI* (-0.79), which indicates a large influence of this parameter on the model performance. However, all other parameters do not show a comparably high correlation. The parameters ~~0.87~~) and *Wind Exposition* (-0.80). Moderately high negative correlations are observed for *Channel Network Distance* ~~Wind Effect~~ (-0.23) and ~~0.50~~, *Positive Openness* (-0.50), *Relative Slope Position* (-0.34) are worth 475 mentioning, ~~0.49~~, and *Channel Network Distance* (-0.45). The only moderately high positive correlation is given for *Valley Depth* with 0.50. All other parameters show low correlation, with values close to zero.

5 Discussion

4.1 Snow distribution mapping in palsa mires and its impacts

480 The snow cover maps provide a high-resolution and precise overview of the distribution within palsa mires. Unique small-scale differences in the height of the snowpack, which are closely related to the topographic properties of the palsa mires, are depicted in ~~SD_{RF}~~ results. However, also ~~SD_{LiDAR}~~ maps provide this kind of differences, although the model results are statistically more accurate.

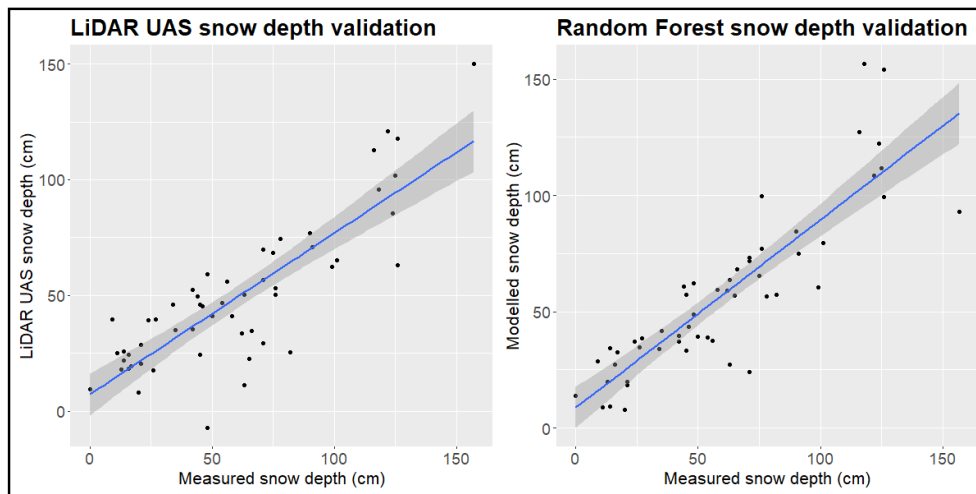


Figure 8. Scatter plots with regression lines for UAS LiDAR-derived and RF-modeled snow depths, based on the external test dataset.

Snow accumulation areas at palsa edges and in open cracks on the palsa tops probably have a warming impact on palsas. This effect is consistent with findings by Peng et al. (2024), who showed that snow accumulation can insulate the ground and reduce cold air penetration. Higher insulation from a dense snowpack reduces the penetration of cold air into the ground during winter. For Pousu palsa (

5 Discussion

5.1 Analysis of RF and LiDAR snow mapping

The statistical analysis of SD_{RF} and SD_{LiDAR} demonstrates statistically significant and reliable results for both approaches. The overall metrics of RMSE and R^2 for RF and LiDAR indicating a slightly better performance of the RF model in mapping snow distribution (Table 3). This trend is also evident in the visual comparison, though a more detailed examination reveals important differences between the two methods. The external validation across all palsa sites confirms the sufficient accuracy of the RF model (Table 3), while the scatter plots (Fig. 8d, e), this effect can be seen at the edges in southwestern and northeastern direction, possibly because of windward and leeward effects. This leads to transportation of snow to these parts following the main wind direction which has been south, southwest during the past 20 years in the Kilpisjärvi area (based on FMI data at Kilpisjärvi weather station). At the bottom of these edges, snow accumulates due to wind and gravitational slide down, leading to a thinner ALT at the edges as the exposition to solar radiation is shorter due to the longer-lasting snow cover. These observations concur with findings by Verdonen et al. (2023) and Seppälä (2011). However, at accumulation zones the frost is not able to penetrate the ground deeply, meaning that the underlying soil is not able to freeze deeply. These parts of a palsa can be classified as warming spots. During late spring and summer) show a strong consistency between the two approaches.

In both approaches, the upper parts of the palsa, which are relatively flat and covered with low vegetation, have similar snow depth values. This is also confirmed by the identical RMSE for the point group *On Top* (Table 4). Since these areas are well represented in the training dataset for the RF approach and the surface captured by UAS LiDAR changes only slightly between summer and winter in the stable area of the palsa, both methods perform well in estimating snow depth. The accuracy of the RF models depends to a large extent on the quality of the training data, which is the reason why a well-distributed dataset is essential. However, these areas remain more humid due to the longer snowmelt, allowing higher temperatures to penetrate deeper because of the higher thermal conductivity and destabilize the ice core especially at edges. Combined with gravitational forces due to the high slope at the edges, block erosion occurs, exposing the frozen core in late spring and summer, which then leads to increased thawing and degradation. These effects are intensified, when cracks open at the upper edge parts and are filled with snow during winter. They can be considered as warming spots as well, which lead to destabilization at the palsa edges. Martin et al. (2021) experimentally showed this in a model approach, pointing out the phase of initial slope adjustment for palsas which constantly experience snow depth between 20–30 cm. According to our findings, even larger depths occur as the surface variations on the top of the palsas are minimal, the acquisition of representative training data is relatively easy, which explains the high accuracy of the model in these areas. The same considerations apply to the UAS LiDAR data. Due to the low vegetation cover, only minimal vegetation removal was required during post-processing, reducing potential sources of error in these areas. However, the seasonal changes in ground level in palsa mires must also be taken into account. Frost heave and subsidence cause natural height variations of several centimeters between summer and winter, as recently described by Renette et al. (2024). If the UAS LiDAR dataset is acquired in spring immediately after snowmelt, when the ALT has reached its minimum thawing depth, such effects could be minimized. In addition, RTK GPS point data from field measurements in winter and summer could help to correct elevation differences by calculating mean elevation shifts. However, this method has its own challenges, as measuring ground level in winter is difficult due to the overlying snow cover. These seasonal variations in elevation should be carefully considered when deriving snow distribution from multi season DTMs. In contrast, RF is expected to be less affected by this problem as the modeled snow depth values are derived from training data and are not directly based on the absolute elevation differences between summer and winter datasets.

Similar patterns are observed for the steep edges of the palsa. While the RF model performs lowest for the *Edge* point class within its own results, the LiDAR approach achieves its second best performance in this category. Despite these internal differences, both methods produce identical RMSE values of 13.12 cm (Table 4). However, when interpreting LiDAR data, there are additional challenges at the palsa edges in the Kilpisjärvi region with increasing degradation. This cycle is repeating until the slopes at the edges are not steep enough to accumulate snow, which happens when the top plateau of a palsa is degrading as well. Snow conditions might have a more significant impact on palsa developments than previously known, as already suggested by Seppälä (2011). Further monitoring and implementation in modeling of the findings of this project can help to better understand the future palsa development, due to continuous degradation processes that lead to differences between the summer and winter DTMs. During summer data collection, palsa edges are recorded before block erosion occurs, meaning that loose soil remains intact. By winter, block erosion and soil displacement may alter the terrain, leading to higher deviations between the DTMs. As a result, the SD_{LiDAR} values are artificially increased even though the actual snow depth is lower. A

similar problem arises if cracks form after data collection in summer, which accumulate snow in winter and further increase the calculated snow depths. At the same time, these degradation processes are also not considered in the RF approach, as the summer dataset was used to derive all input parameters. This explains why RF struggles the most at the edges. In addition, the redistribution and accumulation of snow on steep slopes is a highly dynamic and chaotic process that is difficult to capture with high precision.

On the other hand, cooling spots could also be identified based on the snow distribution. The top parts of the investigated palsas were covered with thin snow layers, allowing frost to penetrate the ground deeply and stabilize the ice core during winter. However, Seppälä (2003) proved that thicker snow cover on palsas prevents melting at the ice core due to a longer duration of snow cover. This means that cooling spots inhibit a greater ALT during summer, where the risk of crack occurrence is higher. As shown for the Pousu palsa (Fig. 8 d, e), the cooling spots are located near to the uppermost parts of steep edges, where the surface is heavily exposed to wind. The assumption is that this, in combination with destabilized and collapsing edges, could lead to very sharp and even vertical edges. The next stage would be the occurrence of cracks, which would lead to more block erosion and degrading. In contrast to other areas of the palsa edge.

Explanation of differences between UAS LiDAR-calculated and RF-modeled snow depths.

5.2 Analysis of RF and LiDAR snow mapping

The statistical analysis of SD_{RF} and SD_{LiDAR} shows that the RF approach outperformed the latter in terms of accuracy. An overall RMSE of 6.16 cm compared to 26.73 cm reveals the better performance of machine learning algorithms compared to the use of not in depth post-processed remote sensing data in snow distribution mapping, shown in Table 3 and Fig. 8. These findings concur with recent studies by Luo et al. (2022) and Panda et al. (2022), the RF and UAS LiDAR approaches show the lowest agreement over open water areas, which is reflected in the statistical metrics for the *Thermokarst* point class. While the RF model estimates snow depth in these areas more accurately than at the palsa edges, UAS LiDAR performs lowest in this category. This can be attributed to the well documented problems with low reflective surfaces such as water (Mandlburger and Jutzi, 2019) and the difficulties in detecting highly scattering materials such as snow (Deems et al., 2013). However, a closer look at the differences provides further insights and helps to understand the results. Figure 5 (b, c) shows, for Pousu palsa, which kind of deviations exist between the two approaches. RF takes advantage of the contextual relationships between the input parameters and the observed snow depth on thermokarst ponds and can therefore compensate for incorrect initial values in the UAS LiDAR dataset and keep a high performance.

It is evident that in both approaches, the upper parts of the palsa, which are mostly flat and populated by low vegetation, contain the same snow cover. High deviations occur in parts characterized by a high slope, higher vegetation, and especially open water. In addition, in mire areas surrounding the palsa, such as the statistics for *Open Area* point class shows it, the RF model performs with the highest accuracy within its own results, while UAS LiDAR ranks second lowest. However, for UAS LiDAR, the deviation from the two best-performing groups *On Top* and *Edge* remains relatively small, indicating a consistent performance across the dataset. A significant challenge in these areas is the seasonal vegetation dynamics. In summer, the vegetation within palsa mires is seasonally taller than during winter due to general growth. In contrast, vegetation-like sedges

570 ~~and grasses is also flattened in winter because in~~ palsa mires grows taller and denser, while in winter the grasses and sedges
~~are compressed under the weight of the snow's weight.~~ The LiDAR sensor ~~detects-records~~ all surface elements, including
~~the vegetation with leaves in summer, but during winter only the snow surface is recorded, leading to a bias between the~~
~~summer and winter DSMs. This existing bias is also detectable in the final snow depth, which means that the snow depth is~~
~~consequently calculated too low i.e. the vegetation in summer and the snow covered areas in winter.~~ Despite the removal of
 575 vegetation in post-processing, a residual bias remains due to the dense vegetation, which cannot be completely filtered out from
the ground, leading to a systematic underestimation of snow depth in areas with height-changing vegetation. height changing
vegetation. Similar problems with LiDAR-derived snow depth mapping were reported by Broxton et al. (2019). Tall shrubs
such as *Betula nana* sometimes, which form thickets at the palsa edges, which could cause problems to detect palsa surfaces
~~with LiDAR. The described problems with precise mapping of snow distribution are also described by Broxton et al. (2019).~~
 580 can further complicate capturing the palsa surface in detail. In contrast, the RF ~~approach incorporates the existing vegetation~~
~~, using the LiDAR-UAS data from summer as a base for all model inherently accounts for vegetation as it uses UAS LiDAR~~
~~summer data as the basis for calculating input parameters. When combining SD_{in-situ} in winter, the RF approach was able to~~
~~connect~~ By integrating SD_{in-situ} measurements from winter, RF can establish relationships between vegetation and higher snow,
~~showeasing the model's strength in calculating these without a high bias-~~ snow accumulation, which reduces bias and improves
 585 snow depth estimation. Methods to further improve LiDAR-derived snow depth mapping, such as correcting estimates based
on vegetation type, density and height, could help to mitigate these limitations.
~~The RF and UAS LiDAR approaches also show high deviations between open water areas—known specifically as thermokarst~~
~~ponds in thawing palsa mires—, although the RF models the snow depth at these parts more precisely than the latter. The low~~
~~performance of the LiDAR sensor can be explained by commonly known problems with low reflecting surfaces such as water~~
 590 ~~(Mandlburger and Jutzi, 2019) or the ability of detecting scattering such as snow (Deems et al., 2013). RF considers the context~~
~~of all parameters in relation to the specific snow depth measured on thermokarst ponds, which explains the strong performance~~
~~of the model even with faulty initial values of the UAS LiDAR data set~~ These results confirm that snow distribution can be
accurately modeled at a small-scale using low cost equipment, such as a yardstick, in combination with moderate computational
resources. However, we acknowledge that an expensive LiDAR sensor was used in this study to derive the input parameters for
 595 the RF model. Therefore, further research should investigate if low cost UAS RGB data can provide equally high quality input
parameters or if LiDAR is still essential for accurate modeling. Recent studies by Harder et al. (2020) and Cho et al. (2024)
have shown that snow depths derived from UAS LiDAR data provide a more accurate representation of snow distribution
than snow depth products derived from UAS RGB data, which raises the question of whether the use of RGB-derived input
parameters is feasible for modeling purposes. However, for large-scale spatial snow distribution overviews or in cases where
 600 high-resolution snow depth mapping is not required, UAS LiDAR or RGB data might be preferable, as manual snow depth
measurements are connected with a high workload and considerable time investment. Furthermore, the potential of UAS
imagery for snow depth estimation has been investigated in several recent studies (Marti et al., 2016; Rauhala et al., 2023; Revuelto et al., 2024),
emphasizing its growing importance for snow distribution monitoring.

5.2 Snow distribution mapping in palsa mires and its impacts

605 The high-resolution snow depth maps produced in this study provide a detailed spatial representation of snow distribution patterns in palsa mires and highlight pronounced warming and cooling areas. Both the LiDAR and RF datasets show similar small-scale variations that are closely linked to topographic features. These findings suggest that the observed snow distribution patterns accurately reflect the actual conditions in the studied palsa landscapes, making them valuable for assessing the potential interactions between snow accumulation and palsa thermal dynamics.

610 ~~Moreover, high deviations at the steep~~ Warming areas in the palsas were identified at the edges of the ~~palsas are visible, here with larger depths calculated by the LiDAR sensor. This can be explained by natural degrading processes at these edges leading to differences between the summer and winter DSMs. For instance, in summer, the edges of the palsas are recorded before block erosion can partly occur and soil can slide to the bottom. In comparison with winter recordings, when block erosion occurs, the LiDAR can detect a high deviation between the DSMs. This results in unnaturally high SD_{LiDAR} , although the actual snow~~

615 ~~depth is lower. The same applies to cracks that can open after the first data collection in summer, leading to higher snow depths in combination with winter data. However, these degrading processes were also not considered in the RF approach since the summer dataset was used for calculating all input parameters, indicating that the RF approach also models the snow depth at edges less accurately (see Table 4 with the most erroneous RMSE at edge parts for the RF approach). Moreover, palsas and in~~ cracks where snow accumulates due to wind transport and gravitational sliding. This effect is consistent with the ~~down-floating~~

620 ~~and accumulating of snow at edges is a chaotic process that is extremely difficult to monitor accurately. Accordingly, a natural shift in ground elevation of several centimetres in palsa mires occurs between summer and winter due to frost heave and subsidence, as Renette et al. (2024) recently described. This should be taken into account when considering snow distribution based on two DSMs from warm and cold seasons~~ findings of Peng et al. (2024), who showed that snow accumulations insulate the ground and reduce the penetration of cold air. An example of this effect can be seen at Pousu Palsa (Fig. 9 d, e), where the

625 ~~dominant south and southwest winds (FMI data for the last 20 years from the Kilpisjärvi weather station) contribute to highest snow accumulation on the southwestern and northeastern edges. Snow accumulation in these areas extends snowmelt into late spring and summer and increases soil moisture, which can increase heat transfer to the soil. While an extended snow cover reduces direct solar radiation, it also prevents deep freezing in winter, which can destabilize ice core edges. This also leads to a thinner ALT at the edges, as the solar radiation remains limited due to the longer-lasting snow cover. These observations~~

630 ~~are consistent with the results of Verdonen et al. (2023) and Seppälä (2011). Such processes can contribute to block erosion and expose the frozen core to further thawing. The formation of cracks in the upper edge zones could also increase this effect, as they fill with snow in winter, delaying freezing and possibly further accelerating the instability of the palsas. These results are consistent with those of Martin et al. (2021), who showed that palsas undergo structural adjustments at constant snow depths of 20-30 cm. However, our results indicate that in the Kilpisjärvi region, even greater snow depths occur at the~~

635 ~~palsa edges, suggesting that the increasing snow accumulation may be linked to the continuing degradation of the palsas. This cycle continues until the palsas slopes flatten, reducing snow accumulation, which eventually leads to the degradation of the upper plateau. Long-term ALT and permafrost temperature measurements at these sites are needed to confirm this~~

hypothesis. As suggested by Seppälä (2011), snow conditions may play a more important role in the development of Palsa than previously thought. Continued monitoring and integration of these findings into permafrost models will be essential for a better understanding of future palsa development.

~~These findings confirm that even with low-cost equipment such as a yardstick and moderate computer power, extremely accurate snow distribution can be modeled on~~ Uppermost parts of the palsa summits are cooling areas, where thin layers of snow allow cold air to penetrate deeper, which promotes ice core stability in winter. Seppälä (2003) proved that a small-scale. We are aware, that in this research an expensive LiDAR sensor was used for preparing input parameter for the RF model.

Therefore, it should be investigated whether a low-cost UAS RGB can provide comparable high-quality input parameters for the model or if expensive LiDAR sensors are necessary. In depth post-processing of the LiDAR dataset, like removing vegetation from the initial point cloud, can help to improve the accuracy of the conducted SD_{LiDAR} to clarify the necessity of an expensive LiDAR sensor. Additionally, it is worth to find out whether a low-cost and low-quality UAS RGB can achieve the same statistical metrics for snow distribution as the UAS LiDAR in order to receive a full understanding about the necessary quality of UAS sensors for snow mapping. For large areas, or if an extremely thicker snow cover on the palsas delays the melting of the ice core due to its prolonged presence. Conversely, this means that cooling areas have deeper ALT in summer than warming areas. As observed at Pousu Palsa (Fig. 9 b, c), the cooling areas are concentrated near the uppermost parts of the steep edges, where the surface is highly exposed to the wind. Further investigation is needed to determine whether this, combined with destabilization and edge collapse, contributes to the formation of steep or even vertical slopes. If this process continues, cracks may eventually form, causing block erosion and degradation of the palsa edge.

The findings of this study suggest that snow depth variability plays a crucial role in the stability of the palsa, with small-scale ; ~~high-precision-overview~~ redistribution patterns influencing local permafrost dynamics. However, as this analysis is only based on snow depth data, further research combining continuous monitoring of snow depth ~~is not needed~~ ; ~~UAS LiDAR or RGB~~ should be the preferred option due to the high workload and time-consuming nature of measuring snow depth. Recently, the potential of UAS imagery for snow depth estimation was explored in several studies (Marti et al., 2016; Rauhala et al., 2023; Revuelto et al. with thermal observations of permafrost is needed to confirm these interactions. Establishing a direct link between snow accumulation patterns and thermal processes in the subsurface would provide valuable insights into the long-term evolution of palsa mires under changing climatic conditions. Furthermore, our study indicates that there is a clear need for more detailed research on the interaction between tall shrubs, snow depth, and permafrost.

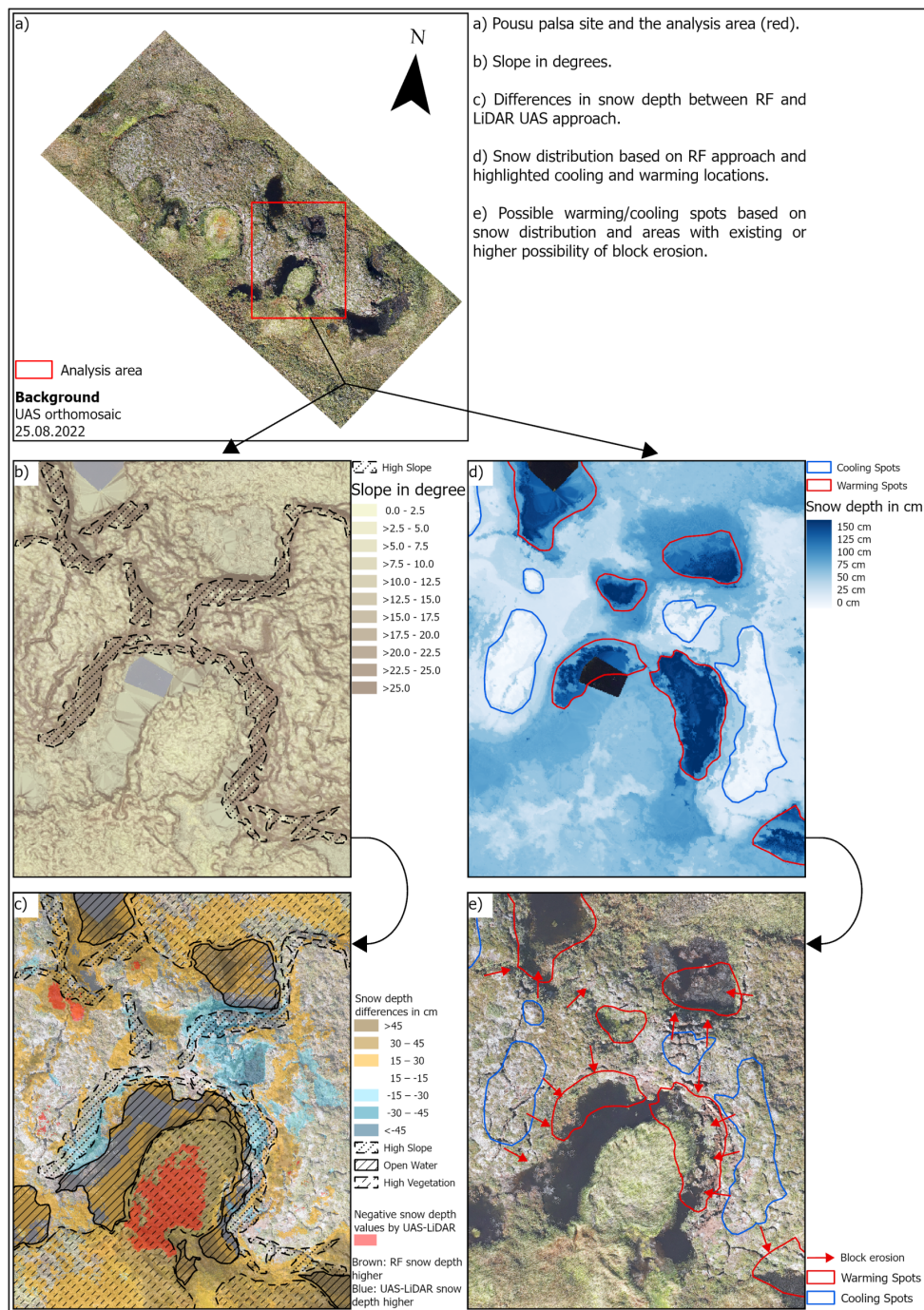


Figure 9. Explanation of differences between UAS LiDAR-derived and RF-modeled snow depths.

~~Snow distribution underlies erratic processes~~ Snow distribution is highly variable, especially because of wind drifts ~~. This and topography, which~~ must be considered when using applying these methods. ~~In addition, these~~ Additionally, machine learning models ~~are based rely~~ on a unique observation in time. Changing weather conditions could ~~lead to result in~~ a completely different snow distribution on another day, which could ~~influence the model quality~~ affect model performance.

670 ~~However, even during the initial collection of the dataset~~ Various sources of error may be present during data collection in summer and winter, ~~errors could have occurred. Especially the LiDAR sensor is prone to errors; surface conditions with high reflectance can lead to dispersion.~~ LiDAR sensors in particular are prone to inaccuracies; highly reflective surfaces can cause scattering of the laser beam and therefore to , leading to a bias in the data . Moreover, not all surface elements can be fully detected due to shielding through shrub vegetation (Gould et al., 2013). This bias must be considered as a consequential error

675 ~~for the whole modeling approach when calculating (Deems et al., 2013). In addition, shrub vegetation can hide the surfaces and prevent them from being fully captured (Gould et al., 2013). These distortions affect the entire modeling approach as they influence the calculation of the input parameters. On the other hand, removing of vegetation in the initial LiDAR-based point cloud could improve the accuracy of SD_{LiDAR}, although it would increase the preparation time clearly. Also the~~ The choice of LiDAR wavelength is another critical factor, as the use of different -or more- wavelengths can increase or multiple

680 wavelengths has been shown to improve the accuracy of snow ~~mapping with LiDAR sensors (Deems et al., 2013). Furthermore, the collection of training data also contains possible errors, although significantly lower. The yardstick is the most reliable method to measure~~ depth mapping (Deems et al., 2013). Errors can also occur when collecting training data, albeit to a less significant extent. Measuring with a yardstick is a reliable method of measuring snow depth, although dense ice layers or near-ground vegetation like roots can alter the

685 but dense layers of ice or vegetation close to the ground, such as roots, can change the recorded values by a few ~~centimetres. The modeling step in RF naturally contains a high susceptibility to errors, such as overfitting. Even if the 10-fold cross-validation detects no significant overfitting, the modeling result can only be exactly verified by using measured snow depth . This should be tested in a first step before applying this method in further projects. Additionally, we have discussed the suitability of all input parameters . It is very plausible that the TPI has such an importance for the model because it summarizes several topographic information in one parameter. Snow accumulates at edges~~

690 and drifts down slopes, meaning in terms of modeling that snow moves from one raster centimeters, as the ground surface was incorrectly assumed. In areas with denser vegetation, the probe may not always reach the exact ground surface, resulting in a slight underestimation of the snow depth. This could affect both the training and validation of the RF model and the accuracy of the LiDAR-derived snow distributions, thus affecting the statistical performance of the results. Devices that have been developed only for taking snow depth values, such as a GPS Magnaprobe, as used in a study by Walker et al. (2021),

695 could minimize such possible errors.

The selection of input parameters is another aspect that requires critical evaluation. The TPI plays a central role in the model as it combines several topographic features into a single parameter. As snow tends to accumulate at the edges and drift down the slopes, its movement from one grid cell to the next . This is perfectly is effectively captured by the ~~TPI~~ TPI, making it a

critical parameter crucial variable for the model. This finding is ~~supported by studies from~~ in line with studies by Revuelto et al.

700 (2020) and Meloche et al. (2022), ~~pointing out which highlight~~ the importance of the ~~TPI~~ TPI for modeling snow distribution.

All other parameters with higher importance are connected to wind characteristics. Other important parameters are related to wind properties and basic surface structures, which supports the significance of wind drifts, emphasizing the importance of wind drift and steep edges in the dynamics of snow distribution formation. However, it should also be noted that the used parameters only represent a small number of available parameters in relation to selected parameters represent only a fraction of the potential variables that influence snow distribution. Theoretically, the RF model is capable of taking a large number of parameters into account and still highlighting theoretically capable of incorporating a larger set of parameters and still identifying the most important ones. Our results also show that changing the input parameters impacts the performance of the model. Accordingly, future work should proceed in the same way, first using a large number of parameters and then successively limiting them to. For example, detailed vegetation classifications - including specific vegetation types or density indices - could further improve snow depth modeling. In addition, there are influencing factors that, while not directly related to snow depth, can still have an impact on snow distribution patterns. The identification of such variables would require a specific study aimed at evaluating and selecting the most important ones. Based on our results, similar projects should consider significantly more parameters, generating better results by including metrics that capture wind and terrain exposure parameters for snow depth modeling.

6 Conclusions

We present an analysis of snow distribution in palsa mires using a combination of field *in-situ* measurements, UAS LiDAR data, and RF-based calculations. This study provides significant valuable insights into small-scale snow dynamics in palsa mires distribution, revealing distinct patterns of snow accumulation at accumulation patterns at palsa edges and cracks of the palsas due to, driven by wind effects and gravitational sliding. The increased snow depth provides thermal insulation, reducing the penetration of cold air during winter and resulting in degradation of frozen soil. Conversely, exposed tops of the palsas in these areas prolongs snowmelt, which could influence thermal insulation and ALT dynamics of permafrost. In contrast, the exposed palsa areas exhibit thinner snow cover, allowing promoting deeper frost penetration but also longer exposition in winter but also greater exposure to solar radiation throughout the year.

Statistically, the RF model demonstrated a high predictive accuracy with a RMSE of 6.16 cm and an R^2 of 0.98, significantly outperforming the UAS LiDAR data, which had in summer. Statistically, both RF modeling and UAS LiDAR provided reliable results for mapping snow distribution with an RMSE of 26.73 cm (LiDAR) and 18.33 cm (RF) and 23.49 cm (LiDAR) and corresponding R^2 values of 0.77 and an R^2 of 0.59. The better performance underscores the effectiveness of incorporating parameters into the model, considering spatial wind- and terrain-related metrics. The *TPI* resulted as the most significant predictor of snow distribution, followed by parameters that consider the influence of wind like *Wind Effect* and *Valley Depth* 0.691. While the RF model showed slightly better prediction performance, the differences between the two approaches remained moderate. This indicates that RF modeling is a promising alternative for snow depth estimation, especially when appropriate input parameters such as *TPI* and wind-related parameters are included. At the same time, UAS LiDAR provides a direct, high-resolution snow depth dataset and is therefore a valuable tool for spatial snow mapping.

Our results ~~underscore~~ highlight the vulnerability of ~~palsas to changing snow dynamics~~ Palsas to changes in snow depth patterns
735 due to climate ~~change. Increasing warming. A change in~~ snow depth and altered wind ~~patterns could intensify palasa degradation~~
~~, leading to the~~ dynamics could further accelerate the degradation of Palsas and lead to a progressive loss of permafrost soils
in ~~Northern~~ northern Finnish Lapland. Future ~~research could expand this high-resolution snow distribution modeling approach~~
~~to larger areas using satellite images, providing more comprehensive insights into the feedback mechanisms~~ studies should
focus on integrating long-term permafrost monitoring with these snow distribution models to better understand the interactions
740 between snow cover, permafrost ~~, thaw~~ and climate change. ~~Our methodology can serve as~~ The presented methodology provides
a foundation for further modeling approaches ~~, integrating knowledge about the importance of snow distribution for palasa~~
~~development with other well-known drivers. It can~~ that integrate snow distribution dynamics with permafrost development.
While tested for palasa environments, the approach can also be applied to other pan-Arctic palasa areas, continuous permafrost
regions, and even ~~for small-scale avalanche forecasting in the Alps. Furthermore, general transferability in other earth surface~~
745 ~~phenomena is given, adapted for small-scale avalanche forecasting or surface process studies~~ such as soil erosion or landform
changes.

In conclusion, this study ~~provides a detailed assessment of snow distribution within palasa mires and its implications for~~
~~permafrost stability. The high accuracy of the RF model underscores the importance of incorporating spatial and environmental~~
~~predictors in snow mapping, showing how small-scale dynamics can be unveiled to improve the understanding of permafrost~~
750 ~~evolution. Additionally, the results can be utilized in greenhouse gas measurements and footprint analyses, among other~~
~~applications, highlighting their relevance for researchers focusing on the interactions between snow cover, permafrost, and~~
~~greenhouse gas emissions~~ demonstrates the feasibility of using both RF modeling and UAS LiDAR for high-resolution snow
depth mapping in palasa mires.

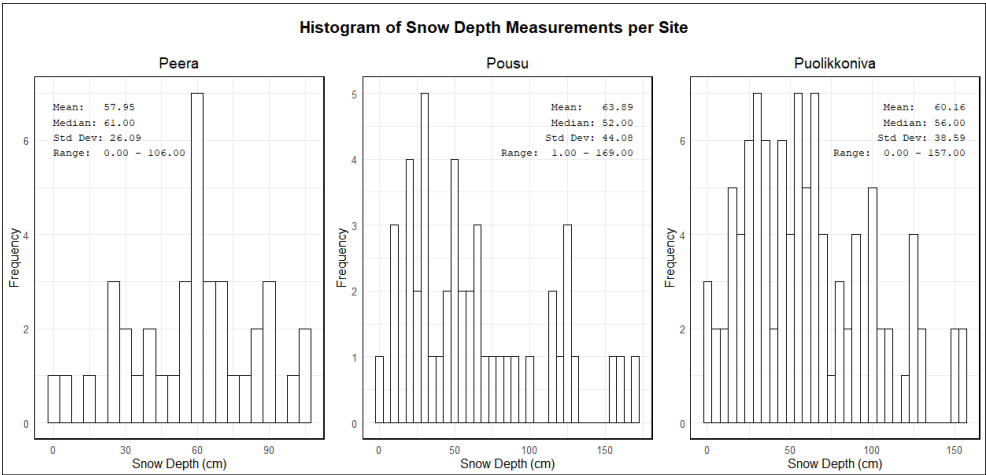


Figure A1. Histogram of SD_{in-situ} points and respective statistics per palsa site.

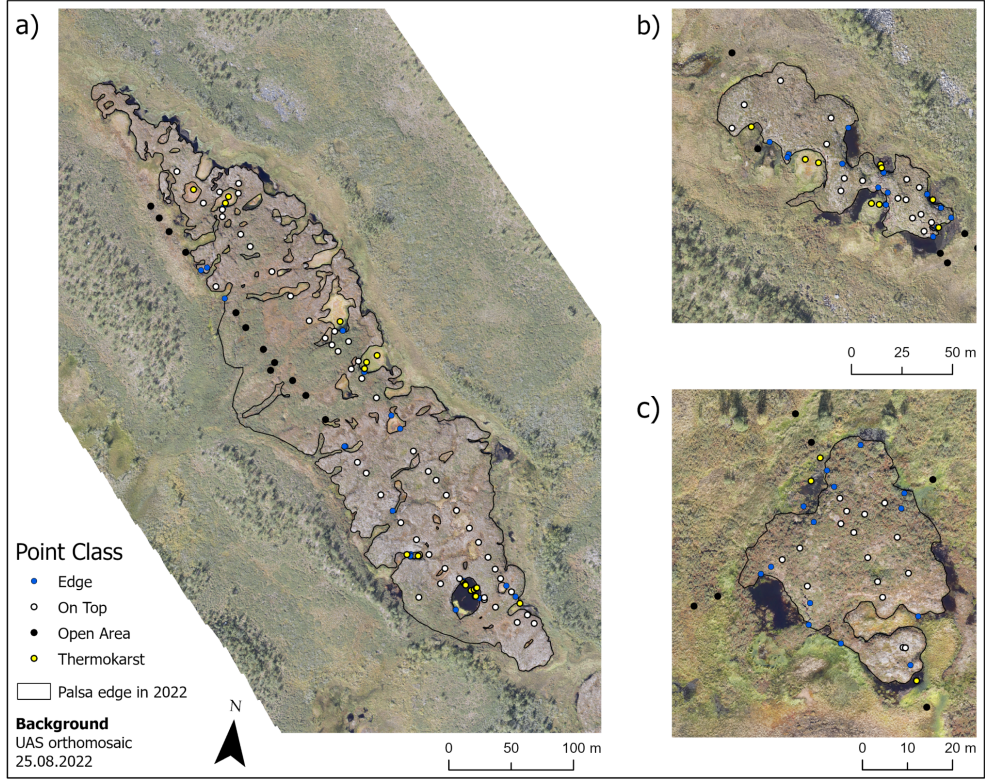


Figure A2. Histogram-Overview of classification of all measured-SD_{in-situ} points into classes Edge, On Top, Open Area and respective statistics of the whole dataset Thermokarst.

Table A1. Correlation between each input parameter and RF-modeled snow depth.

Parameter	Correlation to SD _{RF}	Parameter	Correlation to SD _{RF}
Aspect	0.09	Relative Slope Position	-0.49
Elevation	-0.12	Slope	0.08
Channel Network Base Level	-0.09	Topographic Position Index	-0.87
Channel Network Distance	-0.45	Valley Depth	0.50
Negative Openness	0.22	Wind Effect	-0.55
Positive Openness	-0.50	Wind Exposition	-0.80

Code availability. The R script used in this study is available upon request from the authors.

760 *Data availability.* Snow Depth and UAS data used in this study are available upon request from the authors. Meteorological data are available through the Finnish Meteorological Institute (<https://en.ilmatieteenlaitos.fi/download-observations>, FMI, 2024).

Author contributions. Initial study design: AS. Supervision: BB and TK. Data collection: AS, HS, MV, TK and PK. Data processing: AS, MV and PK. Data analysis and visualization of the results: AS, HS. Discussion of results and conclusions: AS, MV, BB and TK. Writing the paper: AS, with contribution from BB, TK, MV and HS.

Competing interests. The authors declare that they have no conflict of interest.

765 *Financial support.* AS, BB and HS has been supported by the European Union's ERASMUS+ staff mobility programme and by the Graduate Academy of the Leibniz University Hannover. TK, MV and PK were supported by LANDMOD project (the Academy of Finland grant no. 330319) and CHARTER project (EU Horizon 2020 Research and Innovation Programme grant no. 869471).

References

- Autio, J. and Heikkinen, O.: The climate of northern Finland, Fennia, 180, 61–66, 2002.
- 770 Barry, R. G.: The Role of Snow and Ice in the Global Climate System: A Review, *Polar Geography*, 26, 235–246, <https://doi.org/10.1080/789610195>, 2002.
- Bergamo, T. F., de Lima, R. S., Kull, T., Ward, R. D., Sepp, K., and Villoslada, M.: From UAV to PlanetScope: Upscaling fractional cover of an invasive species *Rosa rugosa*, *Journal of Environmental Management*, 336, <https://doi.org/10.1016/j.jenvman.2023.117693>, 2023.
- Bischl, B., Lang, M., Kotthoff, L., Schiffner, J., Richter, J., Studerus, E., Casalicchio, G., and Jones, Z. M.: mlr: Machine Learning in R, 775 <https://github.com/mlr-org/mlr>, 2016.
- Breiman, L.: Random Forests, *Machine Learning*, 45, 5–32, 2001.
- Broxton, P. D., van Leeuwen, W. J., and Biederman, J. A.: Improving Snow Water Equivalent Maps With Machine Learning of Snow Survey and Lidar Measurements, *Water Resources Research*, 55, 3739–3757, <https://doi.org/10.1029/2018WR024146>, 2019.
- Böhner, J. and Selige, T.: Spatial Prediction of soil attributes using terrain analysis and climate regionalisation, *Göttinger Geographische* 780 *Abhandlungen*, 115, 13–28, 2006.
- Bühler, Y., Adams, M. S., Bosch, R., and Stoffel, A.: Mapping snow depth in alpine terrain with unmanned aerial systems (UASs): Potential and limitations, *The Cryosphere*, 10, 1075–1088, <https://doi.org/10.5194/tc-10-1075-2016>, 2016.
- Chai, T. and Draxler, R. R.: Root mean square error (RMSE) or mean absolute error (MAE)? -Arguments against avoiding RMSE in the literature, *Geoscientific Model Development*, 7, 1247–1250, <https://doi.org/10.5194/gmd-7-1247-2014>, 2014.
- 785 Chen, L., Aalto, J., and Luoto, M.: Observed Decrease in Soil and Atmosphere Temperature Coupling in Recent Decades Over Northern Eurasia, *Geophysical Research Letters*, 48, <https://doi.org/10.1029/2021GL092500>, 2021.
- Cho, E., Verfaillie, M., Jacobs, J. M., Hunsaker, A. G., Sullivan, F. B., Palace, M., and Wagner, C.: Characterizing Spatial Structures of Field-Scale Snowpack using Unpiloted Aerial System (UAS) Lidar and SfM Photogrammetry, <https://doi.org/10.5194/egusphere-2024-1530>, 2024.
- 790 Conrad, O., Bechtel, B., Bock, M., Dietrich, H., Fischer, E., Gerlitz, L., Wehberg, J., Wichmann, V., and Böhner, J.: System for Automated Geoscientific Analyses (SAGA) v. 2.1.4, *Geoscientific Model Development*, 8, 1991–2007, <https://doi.org/10.5194/gmd-8-1991-2015>, 2015.
- Deems, J. S., Painter, T. H., and Finnegan, D. C.: Lidar measurement of snow depth: A review, <https://doi.org/10.3189/2013JoG12J154>, 2013.
- 795 DeWalle, D. R. and Rango, A.: Principles of snow hydrology, Cambridge University Press, ISBN 9780511535673, <https://doi.org/10.1017/CBO9780511535673>, 2008.
- EuroGeographics: EuroGlobalMap [data set], <https://www.mapsforeurope.org/access-data>, 2024.
- FMI: Download observations, FMI [data set], <https://en.ilmatieteenlaitos.fi/download-observations>, last access: 09.08.2022, 2022.
- FMI: Seasons in Finland, <https://en.ilmatieteenlaitos.fi/seasons-in-finland>, 2024.
- 800 Gerlitz, L., Conrad, O., and Böhner, J.: Large-scale atmospheric forcing and topographic modification of precipitation rates over High Asia - A neural-network-based approach, *Earth System Dynamics*, 6, 61–81, <https://doi.org/10.5194/esd-6-61-2015>, 2015.
- Gould, S. B., Glenn, N. F., Sankey, T. T., and Mcnamara, J. P.: Influence of a Dense, Low-height Shrub Species on the Accuracy of a Lidar-derived DEM, *Photogrammetric Engineering Remote Sensing*, 79, 421–431, 2013.

- Grohmann, C. H., Smith, M., and Riccomini, C.: Surface Roughness of Topography: A Multi-Scale Analysis of Landform Elements in Midland Valley, Scotland, *Proceedings of Geomorphometry*, pp. 140–148, 2009.
- Gruber, S. and Peckham, S.: Land-surface parameters and objects in hydrology, vol. 33, pp. 171–194, Elsevier Ltd, [https://doi.org/10.1016/S0166-2481\(08\)00007-X](https://doi.org/10.1016/S0166-2481(08)00007-X), 2009.
- Guisan, A., Weiss, S. B., and Weiss, A. D.: GLM versus CCA spatial modeling of plant species distribution, *Plant Ecology*, 143, 107–122, 1999.
- Harder, P., Pomeroy, J. W., Helgason, W. D., and Helgason, W. D.: Improving sub-canopy snow depth mapping with unmanned aerial vehicles: Lidar versus structure-from-motion techniques, *Cryosphere*, 14, 1919–1935, <https://doi.org/10.5194/tc-14-1919-2020>, 2020.
- Hijmans, R. J., van Etten, J., Sumner, M., Cheng, J., Baston, D., Bevan, A., Bivand, R., Busetto, L., Canty, M., Fasoli, B., Forrest, D., Ghosh, A., Golicher, D., Gray, J., Greenberg, J. A., Hiemstra, P., Hingee, K., and Ilich, A.: Package 'raster': Geographic Data Analysis and Modeling, <https://doi.org/10.32614/CRAN.package.raster>, 2023.
- Holmberg, M., Lemmetyinen, J., Schwank, M., Kontu, A., Rautiainen, K., Merkouriadi, I., and Tamminen, J.: Retrieval of ground, snow, and forest parameters from space borne passive L band observations. A case study over Sodankylä, Finland, *Remote Sensing of Environment*, 306, <https://doi.org/10.1016/j.rse.2024.114143>, 2024.
- Hu, J. M., Shean, D., and Bhushan, S.: Six Consecutive Seasons of High-Resolution Mountain Snow Depth Maps From Satellite Stereo Imagery, *Geophysical Research Letters*, 50, <https://doi.org/10.1029/2023GL104871>, 2023.
- IPCC: IPCC, 2023: Climate Change 2023: Synthesis Report. Contribution of Working Groups I, II and III to the Sixth Assessment Report of the Intergovernmental Panel on Climate Change [Core Writing Team, H. Lee and J. Romero (eds.)], <https://doi.org/10.59327/IPCC/AR6-9789291691647>, 2023.
- Jacobs, J. M., Hunsaker, A. G., Sullivan, F. B., Palace, M., Burakowski, E. A., Herrick, C., and Cho, E.: Snow depth mapping with unpiloted aerial system lidar observations: A case study in Durham, New Hampshire, United States, *Cryosphere*, 15, 1485–1500, <https://doi.org/10.5194/tc-15-1485-2021>, 2021.
- James, G., Witten, D., Hastie, T., and Tibshirani, R.: An Introduction to Statistical Learning, <http://www.springer.com/series/417>, 2013.
- Kauhanen, H. O.: Mountains of Kilpisjärvi Host An Abundance of Threatened Plants in Finnish Lapland, *Botanica Pacifica*, 2, 43–52, <https://doi.org/10.17581/bp.2013.02105>, 2013.
- Kiss, R.: Determination of drainage network in digital elevation models, utilities and limitations, *Journal of Hungarian Geomathematics*, 2, 16–29, 2004.
- Kuhn, M.: Building Predictive Models in R Using the caret Package., *Journal of Statistical Software*, 28, 1–26, <https://doi.org/10.18637/jss.v028.i05>, 2008.
- Leppiniemi, O., Karjalainen, O., Aalto, J., Luoto, M., and Hjort, J.: Environmental spaces for palsas and peat plateaus are disappearing at a circumpolar scale, *The Cryosphere*, 17, 3157–3176, <https://doi.org/10.5194/tc-17-3157-2023>, 2023.
- Leppänen, L., Kontu, A., Sjöblom, H., and Pulliainen, J.: Sodankylä manual snow survey program, *Geoscientific Instrumentation, Methods and Data Systems*, 5, 163–179, <https://doi.org/10.5194/gi-5-163-2016>, 2016.
- Luo, J., Dong, C., Lin, K., Chen, X., Zhao, L., and Menzel, L.: Mapping snow cover in forests using optical remote sensing, machine learning and time-lapse photography, *Remote Sensing of Environment*, 275, 113 017, <https://doi.org/10.1016/J.RSE.2022.113017>, 2022.
- Luoto, M., Heikkinen, R. K., and Carter, T. R.: Loss of palsa mires in Europe and biological consequences, <https://doi.org/10.1017/S0376892904001018>, 2004.

- Lépy, E. and Pasanen, L.: Observed regional climate variability during the last 50 years in reindeer herding cooperatives of Finnish Lapland, *Climate*, 5, <https://doi.org/10.3390/cli5040081>, 2017.
- Madani, N., Parazoo, N. C., and Miller, C. E.: Climate change is enforcing physiological changes in Arctic Ecosystems, *Environmental Research Letters*, 18, <https://doi.org/10.1088/1748-9326/acde92>, 2023.
- 845 Mandlbürger, G. and Jutzi, B.: On the feasibility of water surface mapping with single photon lidar, *ISPRS International Journal of Geo-Information*, 8, <https://doi.org/10.3390/ijgi8040188>, 2019.
- Markkula, I., Turunen, M., and Rasmus, S.: A review of climate change impacts on the ecosystem services in the Saami Homeland in Finland, <https://doi.org/10.1016/j.scitotenv.2019.07.272>, 2019.
- Marti, R., Gascoin, S., Berthier, E., Pinel, M. D., Houet, T., and Laffly, D.: Mapping snow depth in open alpine terrain from stereo satellite
850 imagery, *The Cryosphere*, 10, 1361–1380, <https://doi.org/10.5194/tc-10-1361-2016>, 2016.
- Martin, L. C., Nitzbon, J., Scheer, J., Aas, K. S., Eiken, T., Langer, M., Filhol, S., Etzelmüller, B., and Westermann, S.: Lateral thermokarst patterns in permafrost peat plateaus in northern Norway, *The Cryosphere*, 15, 3423–3442, <https://doi.org/10.5194/tc-15-3423-2021>, 2021.
- Meier, K.-D.: Permafrosthügel in Norwegisch und Schwedisch Lapland im Klimawandel, 2015.
- Meloche, J., Langlois, A., Rutter, N., McLennan, D., Royer, A., Billecocq, P., and Ponomarenko, S.: High-resolution snow depth prediction
855 using Random Forest algorithm with topographic parameters: A case study in the Greiner watershed, Nunavut, *Hydrological Processes*, 36, <https://doi.org/10.1002/hyp.14546>, 2022.
- Meriö, L. J., Rauhala, A., Ala-Aho, P., Kuzmin, A., Korpelainen, P., Kumpula, T., Kløve, B., and Marttila, H.: Measuring the spatiotemporal variability in snow depth in subarctic environments using UASs - Part 2: Snow processes and snow-canopy interactions, *The Cryosphere*, 17, 4363–4380, <https://doi.org/10.5194/tc-17-4363-2023>, 2023.
- 860 Merkouriadi, I., Leppäranta, M., and Järvinen, O.: Interannual variability and trends in winter weather and snow conditions in Finnish Lapland, *Estonian Journal of Earth Sciences*, 66, 47–57, <https://doi.org/10.3176/earth.2017.03>, 2017.
- Michele, C. D., Avanzi, F., Passoni, D., Barzaghi, R., Pinto, L., Dosso, P., Ghezzi, A., Gianatti, R., and Vedova, G. D.: Using a fixed-wing UAS to map snow depth distribution: An evaluation at peak accumulation, *The Cryosphere*, 10, 511–522, <https://doi.org/10.5194/tc-10-511-2016>, 2016.
- 865 Nagelkerke, N. J. D.: A note on a general definition of the coefficient of determination, *Biometrika*, 78, 691–692, <https://academic.oup.com/biomet/article/78/3/691/256225>, 1991.
- NOAA: March 2023 Global Snow and Ice Report, <https://www.ncei.noaa.gov/access/monitoring/monthly-report/global-snow/202303>, 2023.
- Olaya, V.: Basic land-surface parameters, vol. 33, pp. 141–169, Elsevier Ltd, [https://doi.org/10.1016/S0166-2481\(08\)00006-8](https://doi.org/10.1016/S0166-2481(08)00006-8), 2009.
- Olaya, V. and Conrad, O.: Geomorphometry in SAGA, vol. 33, pp. 293–308, Elsevier Ltd, [https://doi.org/10.1016/S0166-2481\(08\)00012-3](https://doi.org/10.1016/S0166-2481(08)00012-3),
870 2009.
- Olvmo, M., Holmer, B., Thorsson, S., Reese, H., and Lindberg, F.: Sub-arctic palsa degradation and the role of climatic drivers in the largest coherent palsa mire complex in Sweden (Vissátvuopmi), 1955–2016, *Scientific Reports*, 10, <https://doi.org/10.1038/s41598-020-65719-1>, 2020.
- Panda, S., Anilkumar, R., Balabantaray, B. K., Chutia, D., and Bharti, R.: Machine Learning-Driven Snow Cover Mapping Techniques using
875 Google Earth Engine, in: INDICON 2022 - 2022 IEEE 19th India Council International Conference, Institute of Electrical and Electronics Engineers Inc., ISBN 9781665473507, <https://doi.org/10.1109/INDICON56171.2022.10040153>, 2022.
- Park, H., Fedorov, A. N., Zheleznyak, M. N., Konstantinov, P. Y., and Walsh, J. E.: Effect of snow cover on pan-Arctic permafrost thermal regimes, *Climate Dynamics*, 44, 2873–2895, <https://doi.org/10.1007/s00382-014-2356-5>, 2015.

Peng, X., Frauenfeld, O. W., Huang, Y., Chen, G., Wei, G., Li, X., Tian, W., Yang, G., Zhao, Y., and Mu, C.: The thermal effect of snow cover on ground surface temperature in the Northern Hemisphere, *Environmental Research Letters*, 19, <https://doi.org/10.1088/1748-9326/ad30a5>, 2024.

880 Probst, P., Wright, M. N., and Boulesteix, A. L.: Hyperparameters and tuning strategies for random forest, <https://doi.org/10.1002/widm.1301>, 2019.

Quante, L., Willner, S. N., Middelani, R., and Levermann, A.: Regions of intensification of extreme snowfall under future warming, *Scientific Reports*, 11, <https://doi.org/10.1038/s41598-021-95979-4>, 2021.

885 Ran, Y., Li, X., Cheng, G., Che, J., Aalto, J., Karjalainen, O., Hjort, J., Luoto, M., Jin, H., Obu, J., Hori, M., Yu, Q., and Chang, X.: New high-resolution estimates of the permafrost thermal state and hydrothermal conditions over the Northern Hemisphere, *Earth System Science Data*, 14, 865–884, <https://doi.org/10.5194/essd-14-865-2022>, 2022.

Rauhala, A., Meriö, L. J., Kuzmin, A., Korpelainen, P., Ala-Aho, P., Kumpula, T., Kløve, B., and Marttila, H.: Measuring the spatiotemporal variability in snow depth in subarctic environments using UASs - Part 1: Measurements, processing, and accuracy assessment, *The Cryosphere*, 17, 4343–4362, <https://doi.org/10.5194/tc-17-4343-2023>, 2023.

890 Renette, C., Olmo, M., Thorsson, S., Holmer, B., and Reese, H.: Multitemporal UAV lidar detects seasonal heave and subsidence on palsas, *The Cryosphere*, 18, 5465–5480, <https://doi.org/10.5194/tc-18-5465-2024>, 2024.

Revuelto, J., Billecocq, P., Tuzet, F., Cluzet, B., Lamare, M., Larue, F., and Dumont, M.: Random forests as a tool to understand the snow depth distribution and its evolution in mountain areas, *Hydrological Processes*, 34, 5384–5401, <https://doi.org/10.1002/hyp.13951>, 2020.

895 Revuelto, J., Alonso-Gonzalez, E., Vidaller-Gayan, I., Lacroix, E., Izagirre, E., Rodríguez-López, G., and López-Moreno, J. I.: Intercomparison of UAV platforms for mapping snow depth distribution in complex alpine terrain, *Cold Regions Science and Technology*, 190, <https://doi.org/10.1016/j.coldregions.2021.103344>, 2021.

Richiardi, C., Siniscalco, C., and Adamo, M.: Comparison of Three Different Random Forest Approaches to Retrieve Daily High-Resolution Snow Cover Maps from MODIS and Sentinel-2 in a Mountain Area, Gran Paradiso National Park (NW Alps), *Remote Sensing*, 15, <https://doi.org/10.3390/rs15020343>, 2023.

900 Riley, S. J., DeGloria, S. D., and Elliot, R.: A Terrain Ruggedness Index That Quantifies Topographic Heterogeneity, *Intermountain Journal of Sciences*, 5, 23–27, 1999.

Seppälä, M.: An experimental study of the formation of palsas, <https://www.researchgate.net/publication/255583596>, 1982.

905 Seppälä, M.: Snow Depth Controls Palsa Growth, *Permafrost and Periglacial Processes*, 5, 283–288, 1994.

Seppälä, M.: An experimental climate change study of the effect of increasing snow cover on active layer formation of a palsa, Finnish Lapland, in: 8th Int. Conf. on Permafrost, edited by Phillips, M., Springman, S. M., and Arenson, L. U., pp. 1013–1016, Lisse: Swets Zeitlinger, ISBN 9058095827, 2003.

Seppälä, M.: Palsa mires in Finland, *The Finnish environment*, 23, 155–162, <https://www.researchgate.net/publication/266241369>, 2006.

910 Seppälä, M.: Synthesis of studies of palsa formation underlining the importance of local environmental and physical characteristics, *Quaternary Research*, 75, 366–370, <https://doi.org/10.1016/j.yqres.2010.09.007>, 2011.

Tarini, M., Cignoni, P., and Montani, C.: Ambient Occlusion and Edge Cueing to Enhance Real Time Molecular Visualization, *IEEE transactions on visualization and computer graphics*, 12, 1237–1244, 2006.

Thackeray, C. W. and Fletcher, C. G.: Snow albedo feedback: Current knowledge, importance, outstanding issues and future directions, *Progress in Physical Geography*, 40, 392–408, <https://doi.org/10.1177/0309133315620999>, 2016.

915

- Verdonen, M., Störmer, A., Lotsari, E., Korpelainen, P., Burkhard, B., Colpaert, A., and Kumpula, T.: Permafrost degradation at two monitored palsas mires in north-west Finland, *The Cryosphere*, 17, 1803–1819, <https://doi.org/10.5194/tc-17-1803-2023>, 2023.
- Verdonen, M., Villoslada, M., Kolari, T., Tahvanainen, T., Korpelainen, P., Tarolli, P., and Kumpula, T.: Spatial distribution of thaw depth in palsas estimated from Optical Unoccupied Aerial Systems data, *Permafrost and Periglacial Processes*, 2024.
- 920 Walker, B., Wilcox, E. J., and Marsh, P.: Accuracy assessment of late winter snow depth mapping for tundra environments using structure-from-motion photogrammetry, *Arctic Science*, 7, 588–604, <https://doi.org/10.1139/as-2020-0006>, 2021.
- Walser, H.: Statistik für Naturwissenschaftler, UTB, ISBN 9783825235413, 2011.
- Wang, C., Shirley, I., Wielandt, S., Lamb, J., Uhlemann, S., Breen, A., Busey, R. C., Bolton, W. R., Hubbard, S., and Dafflon, B.: Local-scale heterogeneity of soil thermal dynamics and controlling factors in a discontinuous permafrost region, *Environmental Research Letters*, 19, <https://doi.org/10.1088/1748-9326/ad27bb>, 2024.
- 925 Willmott, C. J. and Matsuura, K.: Advantages of the mean absolute error (MAE) over the root mean square error (RMSE) in assessing average model performance, *Climate Research*, 30, 79–82, <https://doi.org/10.2307/24869236>, 2005.
- Wilson, J. P. and Gallant, J. C.: Primary topographic attributes, pp. 51–85, <https://www.researchgate.net/publication/303543730>, 2000.
- Wood, J.: The Geomorphological Characterisation of Digital Elevation Models, pp. 1–466, 1996.
- 930 Wright, M. N. and Zigler, A.: ranger: A Fast Implementation of Random Forests for High Dimensional Data in C++ and R., *Journal of Statistical Software*, 77, 1–17, <https://doi.org/10.18637/jss.v077.i01>, 2017.
- Yokoyama, R., Shlrasawa, M., and Pike, R. J.: Visualizing Topography by Openness: A New Application of Image Processing to Digital Elevation Models, *Photogrammetric Engineering and Remote Sensing*, 68, 257–265, 2002.
- Zhang, K., Chen, S. C., Whitman, D., Shyu, M. L., Yan, J., and Zhang, C.: A progressive morphological filter for removing nonground measurements from airborne LIDAR data, *IEEE Transactions on Geoscience and Remote Sensing*, 41, 872–882, <https://doi.org/10.1109/TGRS.2003.810682>, 2003.
- 935 Zuidhoff, F. S.: Recent decay of a single palsa in relation to weather conditions between 1996 and 2000 in Laivadalen, northern Sweden, *Geografiska Annaler, Series A: Physical Geography*, 84, 103–111, <https://doi.org/10.1111/1468-0459.00164>, 2002.